AN ABSTRACT OF THE THESIS OF

Kent E. Enfield for the degree of Master of Science in Mechanical Engineering presented on April 7, 2003.

Title: Laminate Mixing in Microscale Fractal-Like Merging Channel Networks

Abstract approved

Redacted for privacy

Deborah V. Pence

A two-dimensional model was developed to predict concentration profiles from passive, laminar mixing of concentration layers formed in a fractal-like merging channel network. Both flat and parabolic velocity profiles were used in the model. A physical experiment was used to confirm the results of the model. Concentration profiles were acquired in the channels using laser induced fluorescence. The degree of mixing was defined and used to quantify the mixing in the test section. Although the results of the experiment follow the trend predicted by the two-dimensional model, the model under predicts the results of the experiment. A three-dimensional CFD model of the flow field in the channel network was used to explain the discrepancies between the two-dimensional model and the experiment.

For the channel network considered, the degree of mixing is a function of Peclet number. The effect of geometry on the degree of mixing is investigated using the two-dimensional model by varying the flow length, the width of the inlet channels, and the number of branching levels. A non-dimensional parameter is defined and used to predict an optimum number of branching levels to maximize mixing for a fixed inlet channel width, total length, and channel depth.

Laminate Mixing in Microscale Fractal-Like Merging Channel Networks

by
Kent E. Enfield

A THESIS

submitted to

Oregon State University

in partial fulfillment of
the requirements for the
degree of

Master of Science

Presented April 7, 2003
Commencement June 2003

Master of Science thesis of Kent E. Enfield presented April 7, 2003

APPROVED:

Redacted for privacy

Major Professor, representing Mechanical Engineering

Redacted for privacy

Head of Department of Mechanical Engineering

Redacted for privacy

Dean of the Graduate School

I understand that my thesis will become part of the permanent collection of Oregon State University libraries. My signature below authorizes release of my thesis to any reader upon request.

Redacted for privacy

Kent E. Enfield, Author

ACKNOWLEDGEMENTS

I would like to thank those who helped me, especially Dr. Deborah Pence, Ali Alharbi, and Jeremy Siekas, and my parents for their support throughout this endeavor.

TABLE OF CONTENTS

1. INTRODUCTION 1

2. LITERATURE REVIEW 4

2.1 USES OF MICRO-SCALE MIXERS 4

2.2 DIFFUSION IN MICRO-SCALE DEVICES 5

2.3 FRACTAL-LIKE NETWORKS 8

3. METHODOLOGY 11

3.1 THE TEST SECTION 11

3.2 ASSUMPTIONS IN NUMERICAL MODELS 13

3.3 TWO-DIMENSIONAL MODEL 14

3.4 THREE-DIMENSIONAL MODEL 19

3.4.1 Grid staggering 19
3.4.2 The SIMPLE method 24
3.4.3 Boundary conditions 26

3.5 PHYSICAL EXPERIMENT 28

3.6 TEST PLAN 33

4. ANALYSIS 39

5. RESULTS 42

5.1 TWO-DIMENSIONAL MODEL FLOW VARIATION 42

5.2 PHYSICAL EXPERIMENT 51

TABLE OF CONTENTS (Continued)

5.3 THREE-DIMENSIONAL CFD 56

5.4 TWO-DIMENSIONAL MODEL GEOMETRY VARIATION 57

6. CONCLUSIONS AND RECOMMENDATIONS 65

REFERENCES 67

APPENDICES 69

LIST OF FIGURES

Figure Page

2.1 Chaotic Mixing 6

2.2 Three-Dimensional Serpentine Channel 7

2.3 Herring-Bone Groove Mixer 8

3.1 Device Geometry 12

3.2 Local Branch Coordinate System 15

3.3 Checkerboard Pressure Solution 20

3.4 Grid Staggering 22

3.5 Index Notation for Staggered Grid 23

3.7 Setup for Physical Experiment 31

3.8 Photograph of Physical Experiment 31

3.9 Intensity-Concentration Calibration Curve 33

5.1 DoM vs. Pe for 2-D model 43

5.2 DoM vs. Pe for 2-D model with high Pe asymptote 45

5.3 DoM vs. Branch Level 47

5.4 Scaled DoM vs. Branch Level 48

5.5 Change in DoM vs. Distance Ratio 50

5.6 Comparison of Experiment and Two-Dimensional Model 52

5.7 False Mixing from a Bent Mixing Zone 54

5.8 DoM vs. Re 54

LIST OF FIGURES (Continued)

Figure Page

5.9 DoM vs. Position 55

5.10 Mixing Layer Streamlines 57

5.11 DoM vs. N for Varying L/h and w_N/h 58

5.12 Π vs. N for Varying L/h and w_N/h 59

5.13 ΔP vs. N for Varying L/h and w_N/h 61

5.14 Pumping Power vs. N for Varying L/h and w_N/h 62

5.15 Ratio of DoM to Pumping Power vs. N for Varying L/h and w_N/h 64

LIST OF TABLES

Table	Page
3.1 Test Section Geometry	12
3.2 Intensity-Concentration Calibration Data	32

LIST OF APPENDICES

APPENDIX A: ERROR ANALYSIS 70

A.1 2-D MODEL 70

A.2 3-D CFD 71

A.3 PHYSICAL EXPERIMENT 71

APPENDIX B: MATLAB CODE 75

B.1 TWO-DIMENSIONAL MODEL 75

B.2 PHYSICAL EXPERIMENT 80

LIST OF SYMBOLS

A	area
C	concentration
d	hydraulic diameter
D	binary mass diffusivity
DoM	degree of mixing. Non-dimensional rms deviation of concentration from average inlet concentration
h	channel depth
I	local image intensity
k	local branching level, varies from 0 to N
L	length
m	limit on summation
n	degree of branching
N	total number of branching levels
P	pressure
Pe	Peclet number Pe = Re*Sc
Q	volumetric flow rate
Re	Reynolds number
Sc	Schmidt number
t	time

u	x-direction component of velocity
U	scaling velocity
v	y-direction component of velocity
V	velocity
w	channel width
x	channel length-wise coordinate
y	channel cross-wise coordinate
z	channel depth-wise coordinate

Greek Symbols

β	ratio of hydraulic diameters of successive branch levels
γ	ratio of lengths of successive branch levels
ν	kinematic viscosity
ρ	density
τ	time step divided by density
ω	relaxation factor
Δ	Euclidean dimension
Δt	time step
Δx	length step in x-direction
Δy	length step in y-direction
ΔP	pressure drop

Π non-dimensional parameter, equal to $((w_N + h)\beta^N - w_N)/L$

Subscripts

0 0^{th} (exit) branch level

ave average

i discretization index in the x-direction

j discretization index in the y-direction

k local branching level

C cross-section

H high value of concentration

L low value of concentration

N N^{th} (inlet) branch level

P pressure

Superscripts

n time index

* intermediate value in SIMPLE method

' correction term in SIMPLE method

+ non-dimensionalized quantity

LAMINATE MIXING IN MICROSCALE FRACTAL-LIKE MERGING CHANNEL NETWORKS

1. INTRODUCTION

Microscale fluid flow devices were originally developed as high capacity heat exchangers for cooling integrated circuits, where heat dissipation is a limiting factor. Soon, other applications, such as chemical analyzers, reactors, biosensors, and fabricators, were found. Many of these applications rely on mixing of different streams to operate. In the analogous macroscale devices, turbulence is usually used to enhance mixing and other transport driven processes.

However, due to their small flow dimensions, it is uncommon for microfluidic devices to achieve turbulent flows, and thus cannot rely on the increased transport properties of turbulence. Also the durability and difficulty of manufacturing the appropriate moving parts at microscales thwarts the use of active mixers, which are common at the macroscale in the form of paddle mixers and the like. Hence micromixers tend to be passive, laminar devices.

While turbulent mixing is difficult to achieve in microscale devices, laminar mixing has an inherent problem. It relies exclusively on molecular diffusion for all the mass transport, which is often too slow for liquids, even in devices with diffusion distances on the order of 100 μm, because of the incredibly low mass

diffusivity of most species in liquids (typically three to four orders of magnitude lower than the diffusivities of momentum or enthalpy).

One way to overcome the problem of low mass diffusivity is to operate over very small diffusion distances. However, reducing the size of the channel to accomplish this either decreases the amount of liquid which can be processed or dramatically increases the required driving pressure if the same throughput is maintained, which is often already a problem in microfluidic devices.

Biological mass transport systems (circulatory and respiratory systems in animals in particular) are able to overcome these problems by using branching/merging fractal like networks. One channel becomes two; two becomes four; four becomes eight; and so on. These networks are able to create in the terminal branches the small distances necessary for molecular diffusion to be effective, while dramatically reducing the required pumping power by having larger diameter channels in the non-terminal branches. One remarkable feature of these biological systems is that the ratios of consecutive hydraulic diameters and branch length are relatively constant across systems (West, Brown, and Enquist; 1997). It is assumed that these ratios are constant because evolution has driven them to an optimal geometry.

One way to minimize the problems of large diffusion distances in larger channels and high pumping power requirements in smaller channels is by building up several thin fluid layers of alternating concentration in a single larger channel, so that mass must only diffuse from one fluid layer to its neighbors, rather than

across the entire channel. This study numerically examines the performance of a fractal-like merging channel network, using consecutive diameter and length scale ratios found in biological systems, as a micromixer over a range of flow rates and mass diffusivities.

2. LITERATURE REVIEW

2.1 USES OF MICRO-SCALE MIXERS

Micro-scale mixing devices have a number of uses. One of them is the manufacture of small devices through the reaction of solutes to form a precipitate. Kenis et al. (1999) describe a fabrication method using laminar flow which they call "FLO". In this method, two (or more) streams of differing chemical composition are brought into contact. The resulting mixing layer is also a reaction zone, and the product precipitates and deposits in the bottom of the channel below the mixing layer. Because the flow is laminar, the mixing layer can be made very thin, and its location can be well controlled. This allows the creation of parts much smaller than the size of the channel in which they are created. Depending on what sort of chemical is deposited, electrochemical, micro-analytical, and micro-synthetic devices can be manufactured.

Another use is as chemical analyzers. Kamholz, Schilling, and Yager (2001) used a T-shaped micromixer to determine the mass diffusivities of several biological compounds. By putting a solution of the substance to be analyzed in one inlet and an indicator that fluoresces in the presence of the analyzed substance in the other, a glowing mixing region was produced. At the low Reynolds numbers used in these analyses, any mixing in the main channel was attributed to molecular

diffusion. By capturing an image of the fluorescing mixture, and comparing the intensity of the fluorescence with a concentration calibration curve, the concentration across the channel was determined. This, along with the known velocity field in the channel, allows the determination of the molecular diffusivity.

Yet another use is as biosensors. Yang et al. (2000) used a micromixer to sort human leukocytes. Applying a non-uniform AC electrical field induces polarization in cells inside the field. The amount of polarization is dependent upon the makeup of the cell, making it strongly dependent on the type of cell. By opposing the resultant electrical forces with gravity, cells can be made to float at different locations in a flow. When the locations are spread across a non-uniform velocity field, such as the parabolic profile inside a microchannel, different types of cells move at different speeds down the channel, sorting them by when they leave the device.

2.2 DIFFUSION IN MICRO-SCALE DEVICES

Because of the small distances involved in micro-scale devices, it is difficult to generate turbulence, either by high Reynolds number flows or by active devices. However, because turbulence is such a strong transport mechanism, much of the research regarding micro-mixers has concentrated on generating turbulent flows in such devices (Ehlers et al., 2000; Ju, 2000).

However, some research has been done on mass transport in micro-scale laminar flows. Ismagilov et al. (2000) observed and quantified broadening of the mixing layer near the walls of the channel. Because of the no-slip boundary condition, the area near the walls is held to very low velocities, increasing the residence time of fluid near the wall and, hence, permitting greater cross-stream diffusion. While this phenomenon probably occurs at all scales, in macro-scale devices the near-wall region of the flow is a much smaller portion of the overall flow, mitigating any effects.

Another area of research is "chaotic mixing" wherein a relatively simple geometry is used to generate a complex flow field, twisting and folding mixing layers, as noted in Figure 2.1, to increase their area and decrease the distances over which diffusion takes place. According to Liu et al. (2000) the flow fields must have at least three independent dimensions. This can be accomplished with either

(a) (b)

Figure 2.1 Chaotic Mixing
(a) shows the distribution of a species without chaotic mixing. Mass must diffuse across the entire channel. (b) shows the distribution after chaotic mixing, but without diffusion. The interfacial region is now much larger, and the distance over which the species must diffuse is greatly diminished.

unsteady flow in a two-dimensional geometry or with steady flow in a three-dimensional geometry. The geometry Liu et al. used was a three-dimensional serpentine channel, similar to that shown in Figure 2.2, which repeated itself. The geometry exhibited superior mixing to both two-dimensional serpentine channels and straight channels.

Stroock et al. (2002) developed a straight-channel chaotic mixer. This was accomplished by placing alternating sections of diagonal grooves in the channel floor to set up cross-channel pressure gradients and hence rotational flow. This design was further improved by replacing the diagonal grooves with asymmetric herring-bone grooves, as shown in Figure 2.3, to set up counter-rotational flow.

Some previous work has been done on improving mixing by lamination: creating zones of different concentrations within the same channel. Branebjerg et al. (1996) developed a device that consists of sections that joined two streams horizontally then split the merged stream in half vertically. Repeating this section three times created sixteen separate fluid layers. The device did achieve complete mixing, but only with flows in which the Reynolds number was less than one.

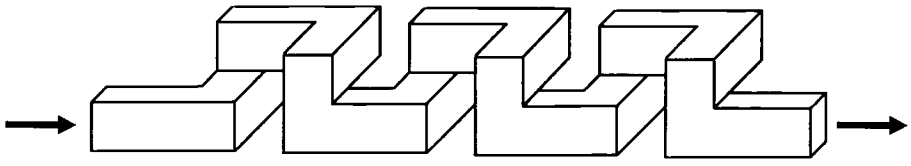

Figure 2.2 Three-Dimensional Serpentine Channel

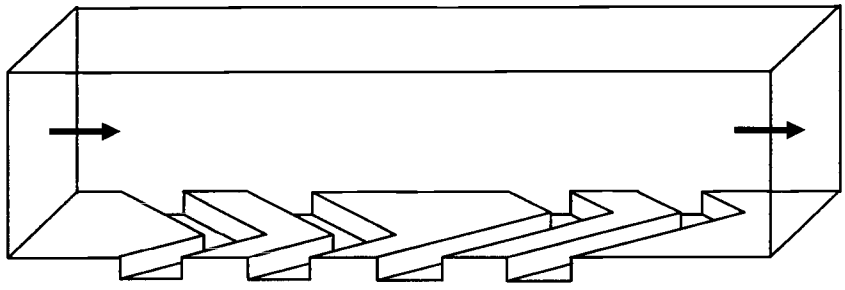

Figure 2.3 Herring-Bone Groove Mixer

Volpert et al. (1999) numerically analyzed an active micromixer. The mixer consists of a large main channel intersecting three smaller cross channels. The cross channels provide cyclical cross flows and are out of phase with each other. The cross channel flows serve to stir the main flow. However, the amount of mixing is quantified by tracking particles of two different types and averaging the type of particle over time and finite areas of the exit. This results in vague descriptions of the mixing, as it is strongly dependent on the number of areas into which the exit is divided.

2.3 FRACTAL-LIKE NETWORKS

The notion of using fractal-like branching networks begins with the observation of natural systems. Nelson et al. (1990) quantify the scaling

relationships between various branch levels of the bronchial tree of the mammalian lung. Analysis of the geometry of lungs from several species shows universal power-law relationships across a range of size-scales of the individual branches.

West et al. (1997) continues the above work by assuming that biological branching transport systems minimize pumping power and that the terminal branches do not vary with body size. From the above assumptions, they conclude that the ratio of hydraulic radii of successive branches is equal to the degree of branching to the minus one-third power, and that the ratio of lengths of successive branches is equal to the degree of branching to negative one over the dimension of the system (two if it is area filling, three if it volume filling). The degree of branching, n, is the number of channels that split from the previous tube, and Δ is the Euclidean dimension of the system (2 if area filling, 3 if space filling).

$$\beta = \frac{d_{k+1}}{d_k} = n^{-1/3} \tag{2-1}$$

$$\gamma = \frac{l_{k+1}}{l_k} = n^{-1/\Delta} \tag{2-2}$$

These results agree with the geometries of natural systems.

Bejan (1997) minimizes the pressure drop under volume constraints in a point to volume branching flow. In order to do so, he concludes that the ratio between diameters of successive branches should be $2^{-1/3}$, except for the ratio between the smallest and second smallest branches where it is $2^{-1/2}$.

Lorente et al. (2002) show that branching flow structures similar to those generated by West et al. can be generated simply by minimizing the path length, rather than fully optimizing all available parameters. They do this for a number of two- and three-dimensional geometries. They show that, for a two-dimensional circular geometry, the channel network generated by minimizing path length requires pumping power of the same order of magnitude as, though somewhat greater than, a geometry generated by optimizing all available parameters to minimize pumping power.

This study investigates passive, laminar mixing in a merging fractal-like channel network with geometry based on the scaling ratios of West et al. (1997). The multiple inlets of the network are use to create alternating layers of high and low concentration, between which mass is transported by molecular diffusion.

3. METHODOLOGY

The device examined in this study is a fractal-like branching channel network used as a micromixer. The performance of the device is analyzed over a range of flow rates and mass diffusivities. The analysis is primarily numerical with a physical experiment to validate the results of the numerical models. There are two numerical models: one is two-dimensional with several simplifying assumptions from which concentration profiles are predicted, while the other is fully three-dimensional and used to determine the three-dimensional flow field through the channel network.

3.1 THE TEST SECTION

A fractal-like branching channel network, originally suggested by Pence 2002, was employed in the present study. It consists of four levels of bifurcation, beyond the initial, 0^{th} level, branch. The geometry of the system mimics that of natural systems, with the ratio of hydraulic diameters between successive levels as $2^{-1/3}$, and the ratio of lengths as $2^{-1/2}$, as suggested by West et al. (1997) for a two-dimensional flow structure. The device, from inlets to the exit plenum, is 16.5 mm radially, and is of uniform depth of 250 microns. The length and width of the 0^{th} level are 5.87 mm and 543 microns, respectively. See Table 3.1 and Figure 3.1.

Table 3.1 Test Section Geometry

Branch Level	Number of Branches	Length [μm]	Width [μm]	Cross-sectional area per branch [mm^2]	Total cross-sectional area for branch level [mm^2]
0	1	5870	543	0.136	0.136
1	2	4151	297	0.074	0.149
2	4	2935	190	0.047	0.190
3	8	2075	130	0.033	0.260
4	16	1468	93	0.023	0.373

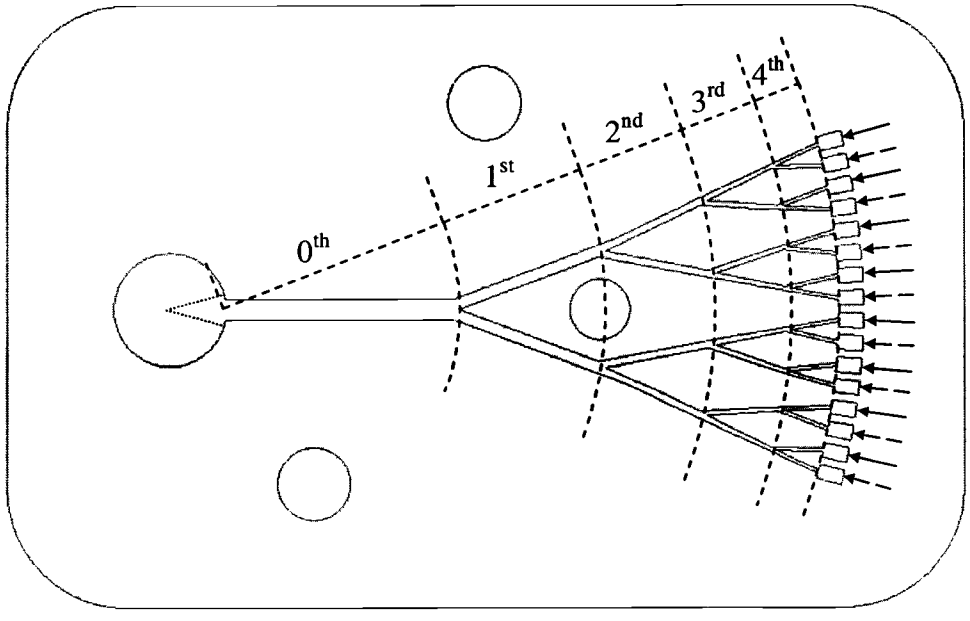

Figure 3.1 Device Geometry
In the physical device and 3-dimensional model, the lengths referred to in Table 3.1 are the distances between the blue arcs. Dye solution enters the plenums marked with solid arrows, and pure water enters the plenums marked with dashed arrows. The dotted lines in the exit plenum represent the location of symmetry boundaries in the three-dimensional CFD model.

This geometry was developed by Pence (2000, 2002) for use as a heat transfer device to cool a surface. In the heat transfer device, analyzed by Alharbi (2001), cool liquid enters the 0^{th} level and exits the fourth level. For use as a mixer the flow is reversed. Flow enters the fourth branch level and exits the 0^{th} level, with equal flow through each branch. The concentrations of the branches of the fourth level alternate between a given concentration of a marker and pure water. The geometry has not been optimized for this application.

3.2 ASSUMPTIONS IN NUMERICAL MODELS

Both numerical models developed for this thesis have a few assumptions in common. The first is that the flow is laminar throughout the entire device. The 0^{th} level has the smallest total cross-section. Thus, by conservation of mass, it has the highest average velocity. In the present investigation, the largest Reynolds number, based on hydraulic diameter, in this level of the network is 1000. Hence, the flow through the 0^{th} level and the entire device is well within the laminar range.

The governing equation for mass transport in a laminar flow with no generation is

$$\frac{\partial}{\partial t}(\rho C)+(\rho \vec{V})\cdot(\vec{\nabla} C)-\vec{\nabla}\cdot(\rho D\vec{\nabla} C)=0 \qquad (3\text{-}1)$$

The flows are steady, eliminating the time derivative term. Because the concentrations are low (the density of the solution is nearly identical to that of the

solvent), the density and viscosity of the solution are assumed to be independent of concentration and equal to those of the solvent. Also, because of the low concentration the mass diffusivity is assumed to be constant. The solvent is water, so the flows are assumed to be incompressible as well. Therefore, the governing equation reduces to

$$\vec{V} \cdot \left(\vec{\nabla} C\right) - D\nabla^2 C = 0 \tag{3-2}$$

Because the density and viscosity of the solution are assumed to be those of the solvent, concentration of the solute does not appear in the momentum and continuity equations, even indirectly. This allows the velocity and pressure fields to be solved independently of, and prior to, the concentration field.

3.3 TWO-DIMENSIONAL MODEL

A model of the branching network was created in Matlab. In this model, the coordinate system is relative to the local branch as seen in Figure 3.2, with x being the lengthwise direction, positive in the upstream direction, and y and z being the spanwise and transverse directions, respectively.

In addition to those stated above, this model makes use of several more simplifying assumptions. The first is that the flow is two-dimensional, eliminating all z derivatives and the z component of velocity. The concentration equation, in Cartesian coordinates, becomes

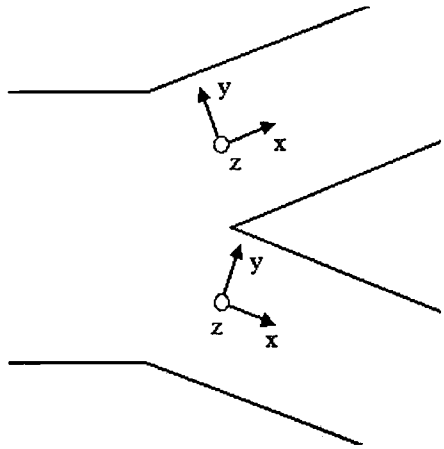

Figure 3.2 Local Branch Coordinate System

$$u\frac{\partial C}{\partial x}+v\frac{\partial C}{\partial y}-D\left(\frac{\partial^2 C}{\partial x^2}+\frac{\partial^2 C}{\partial y^2}\right)=0 \qquad (3\text{-}3)$$

This assumption of two-dimensionality has two notable physical ramifications. One is that the diffusion zones are vertical, with no vertical gradient or mass transfer. The other is that there is no widening of the diffusion zones at the top and bottom of the channel network, as documented by Ismagilov et al. (2000). Both of these effects will reduce the total amount of mixing predicted by the two-dimensional model.

The second simplifying assumption specific to this model is that the velocity field is uniform throughout the device, being either fully-developed (parabolic) or completely undeveloped (constant). It is assumed that when two channels merge, the flow instantly readjusts to the new channel dimensions,

conserving the total mass flow. In either velocity profile, there is no cross-stream velocity component, eliminating the second advection term in the mass transport equation, yielding

$$u\frac{\partial C}{\partial x} - D\left(\frac{\partial^2 C}{\partial x^2} + \frac{\partial^2 C}{\partial y^2}\right) = 0 \tag{3-4}$$

Besides eliminating the effects of a changing velocity profile, this assumption also eliminates any effects resulting from the asymmetry of channel joints observed Figure 3.1. This means that the solution in each channel of a given level (except the fourth level, which requires no solution because the concentration is constant in each channel) will have identical solutions. Hence, only one channel for each level needs to be solved.

Because the mass diffusivities of most species in liquids are very low (typical binary diffusion coefficients are on the order of 10^{-8} to 10^{-10} m^2/s), mass transfer by diffusion occurs many orders of magnitude more slowly than by advection. Therefore, it is assumed in this investigation, as is common in advection-diffusion problems, that diffusion is only relevant when perpendicular to the flow field, eliminating the channel-wise diffusion term. An order of magnitude evaluation of the terms in the equation reveals that streamwise diffusion is two or more orders of magnitude lower than crosswise diffusion as well. The concentration equation becomes

$$u\frac{\partial C}{\partial x} - D\frac{\partial^2 C}{\partial y^2} = 0 \tag{3-5}$$

Because the simplified governing equation is second order in transverse direction and first order in the lengthwise direction, any solution requires three boundary conditions: one length-wise and two cross-wise. For the cross-wise direction, the boundary conditions are impermeable walls. As there is zero mass transport through the walls, mathematically there is zero concentration gradient at the walls.

$$\left.\frac{\partial C}{\partial y}\right|_{walls} = 0 \tag{3-6}$$

Numerically, this is implemented as a second order Newton polynomial,

$$\left.\frac{\partial C}{\partial y}\right|_{walls} = 3C_{i,1} - 4C_{i,2} + C_{i,3} = 0 \tag{3-7}$$

in order to maintain a second order solution scheme in the y-direction. The boundary condition for the length-wise direction is simply the inlet concentration.

$$C|_{entrance} = C(y) \tag{3-8}$$

However, each branching level of the network is considered a separate solution domain in order to handle the changing dimensions of each branch level, so each level requires its own initial concentration. For the fourth branching level, the inlet to the device, each channel has a constant concentration, so the solution is trivial. Two channels from the fourth level, of equal size and flow rate and each of uniform

concentration, join together at the inlet of the third branching level, as seen in Figure 3.1. Therefore the inlet concentration of the third level is simply the concentration of one upstream channel for one half the channel width and the concentration of the other upstream channel for the other half of the channel.

For the 0^{th} through 2^{nd} branch levels, a different approach is required. The simplest approach would be to linearly map the concentration of the previous level onto half the channel width, then again onto the other half. Unfortunately, this simple method does not conserve the mass of the solute. In order to do so the inlet concentration of each level must be mapped to the outlet of the previous level by volume flow rate, not by position. It is a simple matter to numerically integrate the product of the local velocity and local concentration from one wall to any local spanwise position to transform the position coordinate to one of volume flow. The following equation represents the integration

$$\int_0^y vCdy\Big|_{entrance} = \int_0^y vCdy\Big|_{exit} \tag{3-9}$$

where $y_{entrance}$ does not equal y_{exit}. For the discrete quantities in the numerical solution, Equation 3.9 is changed to the following summation

$$\Delta y_{k+1} \sum_j v_{j,k+1} C_{1,j,k+1} = \Delta y_k \sum_j v_{j,k} C_{end,j,k} \tag{3-10}$$

The governing equation itself is numerically implemented via second order centered finite difference approximations

$$u_j \frac{C_{i+1,j} - C_{i-1,j}}{\Delta x} - D \frac{C_{i,j+1} - 2C_{i,j} + C_{i,j-1}}{\Delta y^2} = 0 \qquad (3\text{-}11)$$

and solved by the Gauss-Seidel method.

3.4 THREE-DIMENSIONAL MODEL

The three-dimensional model is constructed in the commercial CFD code Star-CD. It is only used to solve for the flow field, not the concentration field. The geometry of the model matches that of the physical device. Unlike the two-dimensional model, there is no assigned velocity profile. The three-dimensional velocity and pressure fields are solved throughout the flow domain. The governing equations are the steady, incompressible momentum and continuity equations for the velocity and pressure fields.

$$\vec{\nabla} \cdot \vec{V} = 0 \qquad (3\text{-}12)$$

$$\vec{V} \cdot \left(\vec{\nabla} \vec{V}\right) = -\frac{1}{\rho} \vec{\nabla} P + \nu \nabla^2 \vec{V} \qquad (3\text{-}13)$$

3.4.1 Grid staggering

Central finite difference approximations are used to discretize the partial differential equations in order to achieve second order accuracy. These are

$$\frac{\partial f}{\partial x} \approx \frac{f_{i+1,j} - f_{i-1,j}}{2\Delta x} \tag{3-14}$$

$$\frac{\partial^2 f}{\partial x^2} \approx \frac{f_{i+1,j} - 2f_{i,j} + f_{i-1,j}}{\Delta x^2} \tag{3-15}$$

for first and second order x derivatives, respectively. Y-derivatives are similar. Note that the first order derivatives are approximated using values at neighboring locations only. In the governing equations for incompressible flow, Equations 3-12 and 3-13, both pressure and velocity appear in first order derivatives, but velocity also appears in second order derivatives and as first order derivatives multiplied by velocity. Pressure, however, appears only in first order derivatives and is not multiplied by anything but constant fluid properties. Because of this, the value ofthe pressure field is not affected by its nearest neighbors, resulting in the pressure field being broken into two independent groups of cells in a checkerboard pattern as seen in Figure 3.3 . This allows the generation of nonsensical solutions that in no way reflect a physical reality (Tannehill et al., 1997).

One method of avoiding this potential problem is to use a staggered grid. In a staggered grid, scalar quantities are solved for on the original grid, but vector components are staggered in the direction of each vector component. That is, the u-component of velocity is staggered in the x-direction, the v-component is staggered in the y-direction, and the w-component is staggered in the z-direction.

Using the staggered grid, the momentum equations are discretized, and the velocities computed at the staggered grid locations. Thus when applying a central

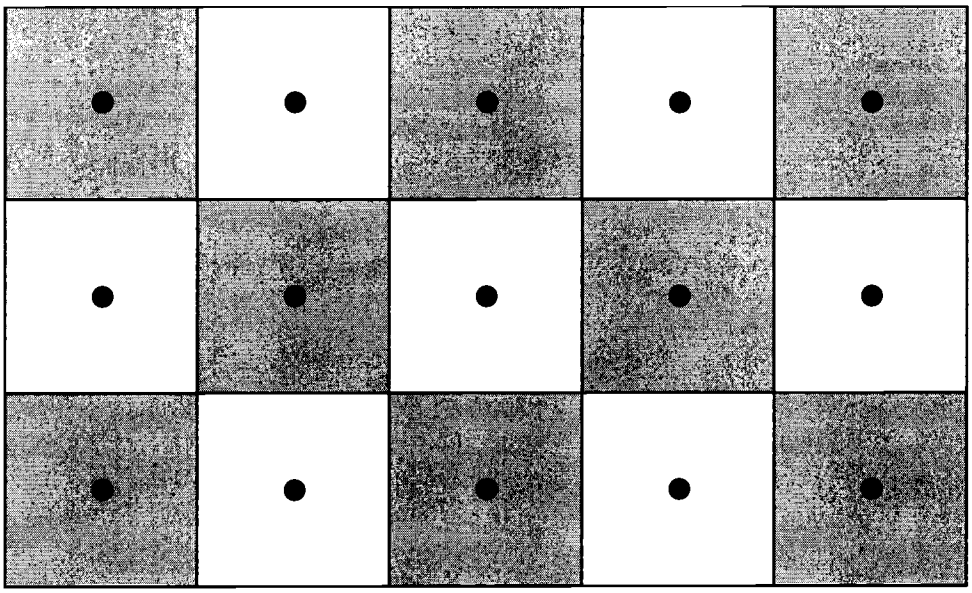

Figure 3.3 Checkerboard Pressure Solution
The solutions of the pressure field in the shaded and unshaded cells are independent of each other.

difference approximation to the pressure terms in the momentum equation, the values of pressure at nodes adjacent to a velocity node are used, as shown in Figure 3.4. These nodes are adjacent pressure nodes, removing the checkerboard disconnection in the pressure field. Where values are not in line with the other quantities in the equation (for example, y-direction velocity in the x-momentum equation), appropriate averages are used (Tannehill et al., 1997). Applying central differences in space and a forward difference in time to the two-dimensional, transient, x-momentum equation yields

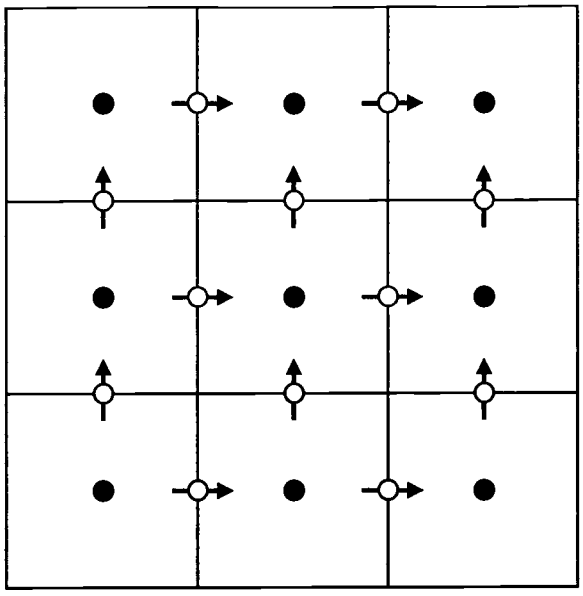

Figure 3.4 Grid Staggering
Scalars are evaluated using cells centered around the black circles. Cells for vector components are centered at the white circles.

$$\rho\left(\frac{u_{i,j}^{n+1}-u_{i,j}^{n}}{\Delta t}+u_{i,j}^{n}\frac{u_{i+1,j}^{n}-u_{i-1,j}^{n}}{2\Delta x}+\overline{v}_{i,j}^{n}\frac{u_{i,j+1}^{n}-u_{i,j-1}^{n}}{2\Delta y}\right)= \\ -\frac{P_{i+\frac{1}{2},j}^{n}-P_{i-\frac{1}{2},j}^{n}}{\Delta x}+\mu\left(\frac{u_{i-1,j}^{n}-2u_{i,j}^{n}+u_{i-1,j}^{n}}{\Delta x^{2}}+\frac{u_{i,j+1}^{n}-2u_{i,j}^{n}+u_{i,j-1}^{n}}{\Delta y^{2}}\right) \tag{3-16}$$

where

$$\overline{v}_{i,j}^{n}=\frac{v_{i+\frac{1}{2},j+\frac{1}{2}}^{n}+v_{i-\frac{1}{2},j+\frac{1}{2}}^{n}+v_{i+\frac{1}{2},j-\frac{1}{2}}^{n}+v_{i-\frac{1}{2},j-\frac{1}{2}}^{n}}{4} \tag{3-17}$$

is the appropriately averaged value for v. The equation is centered about u-velocity node i,j noted in Figure 3.5. Similar equations can be created for the other momentum equations and for three-dimensional flows.

The scalar equations for continuity and concentration are centered about the scalar nodes, represented by the black circles in Figure 3.5. By using the transient equation to solve a steady flow with a given pressure field, it is straightforward to solve for the velocity field by marching forward in time until the solution converges with the time derivative approaching zero.

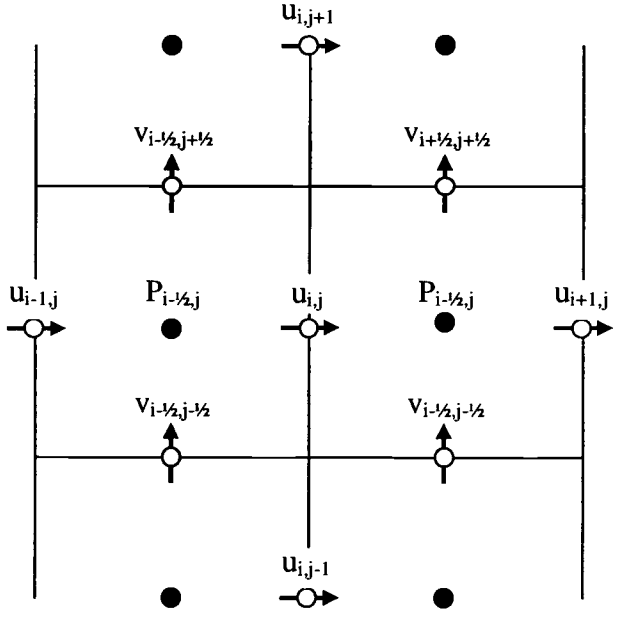

Figure 3.5 Index Notation for Staggered Grid

3.4.2 The SIMPLE Method

The SIMPLE (semi-implicit method for pressure linked equations) method is a solution scheme that makes use of alternately solving the pressure field, solving the velocity field, and correcting the pressure and velocity fields. It was developed by Patankar and Spalding in 1972 as noted in Tannehill, Anderson, and Pletcher (1997)

In this method is assumed that the actual pressure is made up of an intermediate value (P^*) and a correction (P'):

$$P = P^* + P' \tag{3-18}$$

The velocity components are decomposed similarly:

$$u = u^* + u' \tag{3-19}$$
$$v = v^* + v' \tag{3-20}$$
$$w = w^* + w' \tag{3-21}$$

The pressure correction is related to the velocity corrections by approximate forms of the momentum equations

$$\rho \frac{\partial \vec{V}'}{\partial t} = -\vec{\nabla} P \tag{3-22}$$

Because the velocity corrections at the previous iteration can be assumed to be zero, the above equations can be rewritten as

$$\vec{V}' = -\tau\vec{\nabla}P' \tag{3-23}$$

where τ is a time increment divided by density. By substituting the above relationships into the velocity decompositions and substituting the results into the continuity equation yields the following straightforward Poisson equation:

$$\nabla^2 P' = \frac{1}{\tau}\vec{\nabla}\cdot\vec{V}^* \tag{3-24}$$

This equation can be easily discretized and solved numerically.

The SIMPLE method consists of the following steps:

1. Guess a solution to the pressure field.

2. Use that pressure field to solve for the velocity field, using the staggered grid and procedure described above.

3. Solve the pressure correction equation.

4. Correct the pressure and velocity fields. The pressure derivatives in the equations for the velocity corrections are easily discretized.

$$u = u^* - \frac{\tau}{2\Delta x}\left(P'_{i+1,j,k} - P'_{i-1,j,k}\right) \tag{3-25}$$

$$v = v^* - \frac{\tau}{2\Delta y}\left(P'_{i,j+1,k} - P'_{i,j-1,k}\right) \tag{3-26}$$

$$w = w^* - \frac{\tau}{2\Delta z}\left(P'_{i,j,k+1} - P'_{i,j,k-1}\right) \tag{3-27}$$

5. Check for convergence and return to Step 2 if unconverged.

In practice, the pressure correction equation often overestimates P′, slowing down the convergence of the solution. Because of this, an underrelaxation factor is often introduced when correcting the pressure field

$$P = P' + \omega_p P' \tag{3-28}$$

For similar reasons, the momentum equations are often underrelaxed as well, by changing the parameter τ. A flowchart of the SIMPLE method is shown in Figure 3.5.

3.4.3 Boundary conditions

In the model, there are four types of boundaries, providing the necessary boundary conditions for the governing equations. The first is the inlet type. They are located at the inlets of each of the 4^{th} level branches, shown in Figure 3.1. Inlet boundaries have specified velocity and density. The velocity fields are defined as uniform flow, directed straight into the channel. This is chosen because in the physical device, the flow enters the device from small plenums, and the true velocity distribution at this location is unknown. The density is that of water.

The second boundary type is wall. The walls are defined as stationary and immobile. The no-slip boundary condition restricts velocity to zero at the wall.

The third type is the pressure boundary, which allows flow to cross the boundary in any direction. This allows for recirculation through the boundary.

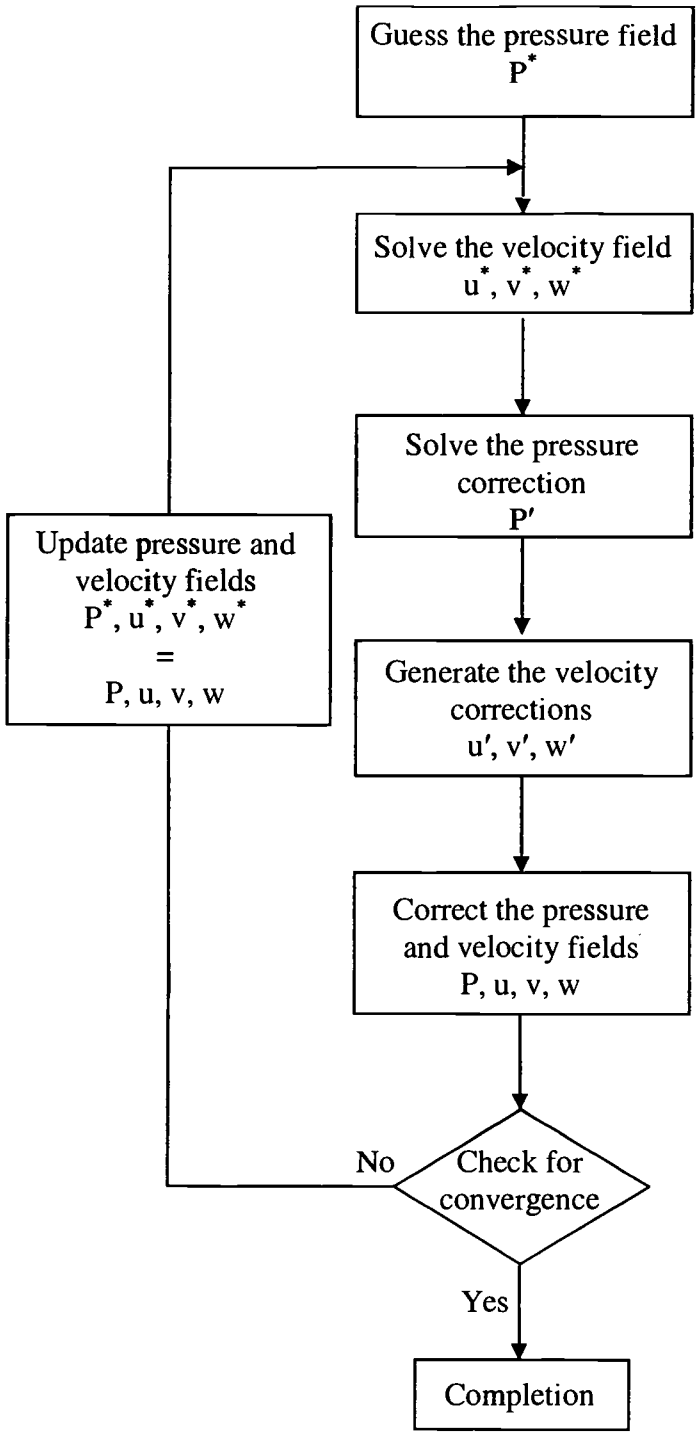

Figure 3.6 Flowchart of the SIMPLE Method

This is used at the outlet of the device. A pressure boundary simply assigns a value to pressure at the boundary. This is linked with the local pressure gradient, and when combined with the continuity equation effectively prescribes the velocity. In the model, it is assumed to be ambient atmospheric. In the physical device, this would not be true, as the device is not vented directly to atmosphere, but as the absolute pressure is not important, it is acceptable.

The fourth type is the symmetry boundary. This is used at the vertical sides of the exit area, composing one twelfth of the exit plenum as noted by the dotted lines in Figure 3.1. In the physical device, this is a plenum in which twelve identical 0^{th} level branches merge. The symmetry boundary uses standard symmetry conditions: zero gradients of all quantities perpendicular to the boundary.

The equations are discretized using the second order MARS method, and solved using the SIMPLE method, which makes uses of staggered grids to solve for vector quantities. The scalar quantities are solved for using the default grid. Vector components in the x direction are solved for on a grid staggered in the x-direction, components in the y-direction on a grid staggered in the y-direction, and z-components on a grid staggered in the z-direction.

3.5 PHYSICAL EXPERIMENT

The results of the numerical models are compared to those from a physical experiment. Measurements of the concentration are taken by illuminating

rhodamine 6 chloride with a laser and capturing the image with a charge coupled device (CCD) camera. The intensity of the fluorescence is then converted into the local concentration via a calibration curve.

The setup of the physical experiment consists of two main sections: the flow loops and the optical setup. The two portions intersect and interact at the mixer test device. The micromixer test section is fabricated using laminate construction. The main layer is a 250 micron thick piece of polycarbonate, out of which the branching channel network has been cut. Above and below this layer are thick layers of polycarbonate, in which the plenums for the dye solution and pure water are cut, which serve as stiffeners. These three layers are thermally bonded together using an mechanically applied pressure.

The exit plenums of the experimental test section and the CFD model differ somewhat. As can be seen in Figure 3.1, in the physical experiment, only one 0^{th} level channel exits into a circular plenum. In the CFD model, it was assumed that twelve such channels exit into the same plenum.

The test section was held in an aluminum combination mounting bracket and manifold with two gaskets. The mounting bracket is secured with six bolts. The assembled device is mounted on a translation platform to allow precise control of its location relative to the camera and laser beam.

The flow loop portion of the setup begins with a syringe pump (Cole Parmer 74900 series) that provides equal flow rates of water and dye solution from separate syringes (Hamilton Co. Gastight ® 1010) to the mixer through 1/8" inner

diameter tubing (Kuri Tec K010 from Kuriyama). The two flows join in the micromixer. The outlet of the device is connected to a waste reservoir with more of the same tubing.

For the physical experiment, rhodamine 6G chloride (from Molecular Probes) is used as the solute because of its absorption and emission characteristics. It absorbs light at a peak wavelength of 525 nm and emits it at a peak of 560 nm. Its binary diffusion coefficient is specified as 2.8×10^{-10} m^2/s by the supplier.

The optical portion of the setup starts with an argon laser (Lexel Model 85), which has a wavelength of 480 to 512 nm, used to illuminate and excite the rhodamine. The laser is aimed at a beam splitter with a mirror and diverging lens system. Aiming the laser into the beam splitter allows the beam to be aimed in the same direction as the camera, eliminating shadows. The beam excites the rhodamine, which fluoresces. A Melles Griot sharp cutoff filter is located between the beam splitter and the camera. It has a nominal cutoff at 550 nm and maximum transmission at 615 nm. It filters out any reflected light from the laser, allowing the CCD camera (Panasonic GPUS5328) to take an image of only the light emitted by the fluorescing rhodamine. A series of six images were captured with a PCI 1408 image capture board. They were then averaged and filtered using Matlab. A schematic and a photograph of the experimental setup are shown in Figures 3.6 and 3.7, respectively.

Once images were taken of the flow, they were converted into concentration data using an experimentally determined calibration curve. A 10^{-5} M solution of

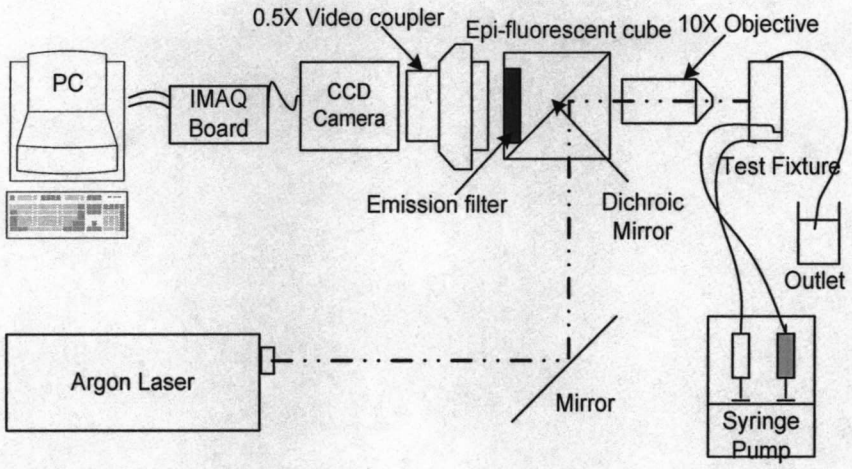

Figure 3.7 Setup for Physical Experiment

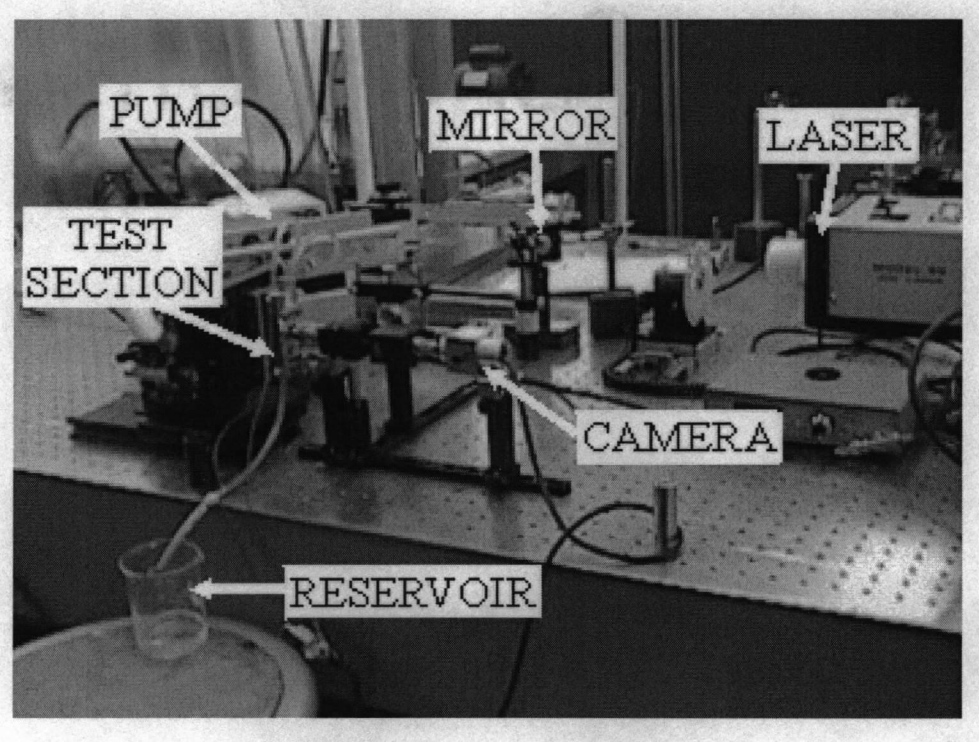

Figure 3.8 Photograph of Physical Experiment

rhodamine was diluted from 100 percent down to 0 percent in 10 percent intervals. For each of these steps, the same concentration of rhodamine was injected into each set of inlets, and images of the constant concentration flow were taken. The intensity of these images and the associated known concentrations, given in Table 3.2, were used to generate a curve of concentration as a function of image intensity using Matlab. Because the solution fluoresces, it does not follow the linear nature of the Beer-Lambert law. The equation for the fitted curve is

$$C = 3.52\times10^{-5} I^{1.98} \tag{3-29}$$

Table 3.2 Intensity-Concentration Calibration Data

Concentration	Intensity
0.000	0.6
0.100	49.8
0.200	76.9
0.299	101.2
0.400	112.2
0.500	129.8
0.600	137.1
0.699	151.0
0.800	152.7
0.900	166.3
1.000	178.0

The concentration is scaled as a fraction of 10^{-5} M. Image intensity is on a scale of 0 to 255.

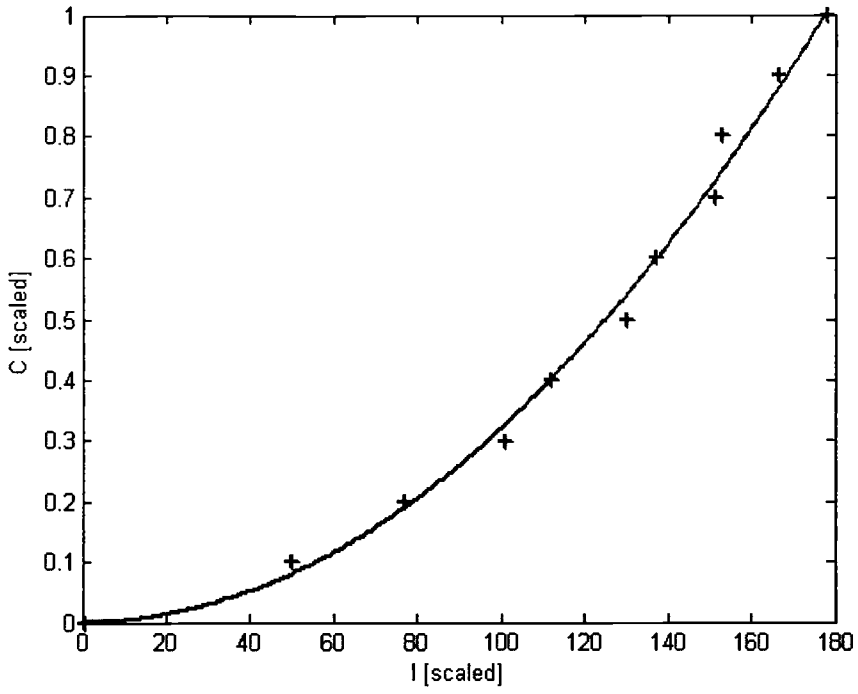

Figure 3.9 Intensity-Concentration Calibration Curve

The data and fitted curve are plotted in Figure 3.8

3.6 TEST PLAN

Starting with the simplified form of the advection-diffusion mass transport equation used in the two-dimensional model

$$u\frac{\partial C}{\partial x} - D\frac{\partial^2 C}{\partial y^2} = 0 \tag{3-29}$$

and introducing the non-dimensional scaled variables

$$u^+ = \frac{u}{U}, \quad C^+ = \frac{C - C_L}{C_H - C_L}, \quad x^+ = \frac{x}{L}, \quad y^+ = \frac{y}{w} \tag{3-30}$$

or

$$u = u^+ U, \quad C = C^+ (C_H - C_L) + C_L, \quad x = x^+ L, \quad y = y^+ w \tag{3-31}$$

the resulting equation is

$$u^+ U \frac{\partial \left(C^+ (C_H - C_L) + C_L \right)}{\partial \left(x^+ L \right)} - D \frac{\partial^2 \left(C^+ (C_H - C_L) + C_L \right)}{\partial \left(y^+ w \right)^2} = 0 \tag{3-32}$$

Removing the constant reference length and concentration difference from the derivatives gives

$$\frac{u^+ U (C_H - C_L)}{L} \frac{\partial C^+}{\partial x^+} - \frac{D (C_H - C_L)}{w^2} \frac{\partial^2 C^+}{\partial y^+} = 0 \tag{3-33}$$

A trivial amount of algebra yields

$$u^+ \frac{\partial C^+}{\partial x^+} - \frac{DL}{Uw^2} \frac{\partial^2 C^+}{\partial y^{+2}} = 0 \tag{3-34}$$

Introducing the Peclet number, which is the ratio of transport by advection to transport by diffusion (as can be seen in both its definition and the final equation),

$$Pe = \frac{wU}{D} \tag{3-35}$$

finally yields

$$u^+ \frac{\partial C^+}{\partial x^+} - \frac{1}{Pe} \frac{L}{w} \frac{\partial^2 C^+}{\partial y^{+2}} = 0 \tag{3-36}$$

A similar procedure can be performed for the fully three-dimensional advection-diffusion equation, resulting in

$$\vec{V}^+ \cdot \left(\vec{\nabla}^+ C^+ \right) - \frac{1}{Pe} \nabla^{+2} C^+ = 0 \tag{3-37}$$

where

$$\vec{\nabla}^+ = \left\langle \frac{\partial}{\partial x^+}, \frac{L}{w} \frac{\partial}{\partial y^+}, \frac{L}{h} \frac{\partial}{\partial z^+} \right\rangle \tag{3-38}$$

It can be seen that the concentration field depends primarily on the Peclet number, with any separate Reynolds number dependence entering through the velocity field. In the case of the two-dimensional model, the imposed velocity fields do not change shape (only magnitude) with Reynolds number, being either parabolic or flat. Fifteen values for Peclet number are used, ranging from 100 to 170,000,000 in non-equal increments.

In the physical experiment only one value for Schmidt number (that of the fluorescent dye) is available, so Reynolds number cannot be varied independently

of Peclet number. The range of values for the Reynolds number are limited because at low Reynolds number so much mixing occurs that the concentration becomes nearly constant across the channel, and at moderately high Reynolds number the pressure drop through the device becomes more than the device can withstand and it begins to leak. Reynolds number was varied from 2 to 20 in increments of 2 and from 25 to 50 in increments of 5.

The three-dimensional CFD model was used to investigate the velocity field inside the test section. Reynolds numbers investigated were 1, 5, 10 and 50.

The geometry of the channel network also affects the amount of mixing that takes place, so it too should be varied. There are six parameters that define the fractal geometry, and they are used in a parametric study. They are the total length, L, the width of the smallest channel, w_N, the depth of the channel, h, the number of branchings, N, the ratio of hydraulic diameters of successive branches, β, and the ratio of lengths of successive branches, γ. N, β, and γ are already dimensionless, while L, w_N, and h all have dimensions of length, so they can be formed into two dimensionless groups, L/h and w_N/h, for a total of five dimensionless groups defining the network geometry.

β and γ are assumed to be already at their optimum values, so they will not be varied. This leaves only N, L/h, and w_N/h to be varied. Keeping h constant at 250 μm for convenience and consistency with the existing geometry used for varying Peclet number, leaves three independent parameters, L, w_N, and N. L is

varied from 5 mm to 25 mm in 5 mm increments, w_N is varied from 50 μm to 250 μm in 50 μm increments, and N is varied from 1 to 5.

This gives an array of 125 geometries. However, solving for width the definition of hydraulic diameter for a rectangular channel yields:

$$d = \frac{2wh}{w+h} \Leftrightarrow w = \frac{dh}{2h-d} \tag{3-39}$$

Note that the hydraulic diameter approaches twice the height of the channel as the width of the channel becomes very large. Introducing the definition of beta, one can write the width of the 0^{th} channel in terms of the N^{th} channel width.

$$w_0 = \frac{w_N h}{(w_N + h)\beta^N - w_N} \tag{3-40}$$

For w_0 to be sensical (finite and positive), the denominator of the right-hand side of the above equation must be greater than zero, or after some rearranging

$$\beta^N > \frac{w_N}{w_N + h} \tag{3-41}$$

This constraint eliminates several of the proposed 125 geometries. Further limiting the geometries such that $w_k < L_k$ eliminates several more. The following geometries are not used in the parametric study:

- N = 3, w_N = 200 microns, and L = 5 mm
- N = 3, w_N = 250 microns, all lengths
- N = 4, w_N = 150 microns, and L = 5 or 10 mm
- N = 4, w_N = 200 or 250 microns, all lengths
- N = 5, w_N = 100 microns, and L = 5 mm
- N = 5, w_N = 150, 200, or 250 microns, all lengths

Eliminating these geometries leaves 91 different geometries.

The Reynolds number and Peclet number are held constant at 10 and 5000, respectively.

4. ANALYSIS

The main objective of this research is to determine and characterize the amount of mixing that has occurred as a function of flow rate and mass diffusivity, not just to produce a concentration profile at the outlet of the mixer, though the two items are strongly related. If no diffusion occurs, despite contortion and intertwining of the initial streams, the concentration everywhere would be identical to the concentration of one inlet or the other. If complete mixing occurs, the concentration everywhere would be the arithmetic mean of the two inlet concentrations, as there is equal mass flow rate.

To characterize the amount of mixing, the integral across the cross section of the root-mean-square (RMS) deviation from the mean concentration,

$$\left\{\frac{1}{A_c}\iint_{A_c}\left[C-\tfrac{1}{2}(C_H+C_L)\right]^2 dA\right\}^{\frac{1}{2}} \tag{4-1}$$

can be used. The use of the RMS avoids a problem inherent in simply integrating the concentration, which is that the integral would have the same value regardless of the concentration field as there is the same amount of solute exiting the device, no matter how it is distributed. Integrating the deviation from the mean concentration has the same problem.

Unfortunately, the RMS deviation depends on the inlet concentrations. To make comparisons of results from one flow to another meaningful, the value used to characterize the amount of mixing should be non-dimensional and independent of the inlet concentrations. To accomplish this, in the present analysis the rms deviation is scaled by the mean concentration:

$$\frac{\left\{\frac{1}{A_c}\iint_{A_c}\left[C-\frac{1}{2}(C_H+C_L)\right]^2 dA\right\}^{\frac{1}{2}}}{\frac{1}{2}(C_H+C_L)} \tag{4-2}$$

However, this gives a counter intuitive scale with 0 being complete mixing and 1 being no mixing. So this number is subtracted from one, to make 0 represent no mixing and 1 represent complete mixing. It is referred to as the degree of mixing (DoM), and is defined as:

$$DoM = 1-\frac{\left\{\frac{1}{A_c}\iint_{A_c}\left[C-\frac{1}{2}(C_H+C_L)\right]^2 dA\right\}^{\frac{1}{2}}}{\frac{1}{2}(C_H+C_L)} \tag{4-3}$$

Liu et al. (2000) use a similar RMS based quantification of mixing, but use the image intensity directly without converting it to concentration. They also use the difference between the local intensity and the maximum, rather than the average.

For the discrete numerical models, the continuous integral changes to a sum over finite areas, as shown by:

$$DoM = 1 - \frac{\left\{ \frac{1}{A_c} \sum_{j=1}^{m} \left[C_i - \frac{1}{2}(C_H + C_L) \right]^2 A_i \right\}^{\frac{1}{2}}}{\frac{1}{2}(C_H + C_L)} \tag{4-4}$$

In the two-dimensional model, the degree of mixing is reduced from a sum over areas to a sum over lengths. With the constant grid-spacing of the model, the individual lengths come out of the sum, where they cancel the total length, leaving

$$DoM = 1 - \frac{\left\{ \frac{1}{m} \sum_{j=1}^{m} \left[C_j - \frac{1}{2}(C_H + C_L) \right]^2 \right\}^{\frac{1}{2}}}{\frac{1}{2}(C_H + C_L)} \tag{4-5}$$

Note, however, that due to the nonlinear nature of the intensity curve discussed in section 3.5, the average concentration in a measured concentration profile may not be the same as the average of the inlet concentrations. Thus it is appropriate to replace the average inlet concentration with the measured average concentration in the definition of DoM, as given by

$$DoM = 1 - \frac{1}{C_{ave}} \left\{ \frac{1}{m} \sum_{j=1}^{m} \left[C_j - C_{ave} \right]^2 \right\}^{\frac{1}{2}} \tag{4-6}$$

5. RESULTS

The concentration results from the two-dimensional model and physical experiment are compared. The discrepancies in concentration distribution between the results of the two-dimensional model and experiment are explained by the three-dimensionality of the flow field generated using CFD.

5.1 TWO-DIMENSIONAL MODEL FLOW VARIATION

The results of the two-dimensional model can be seen in Figure 5.1, which shows the degree of mixing versus Peclet number along with a curve fitted to the data. The curve is

$$DoM = \left(1 + 8.0 \times 10^{-5} Pe\right)^{-0.54} \tag{5-1}$$

The curve was fit by minimizing, in a least squares sense, the difference between the log based 10 of the data and the log based 10 of the curve. Because of the non-linear form of the equation, the minimum in the error must be found numerically rather than analytically. This is done with a gradient based optimization scheme (Chapra and Canale, 1998). The step-size is refined until the solution changes by less than 0.1%.

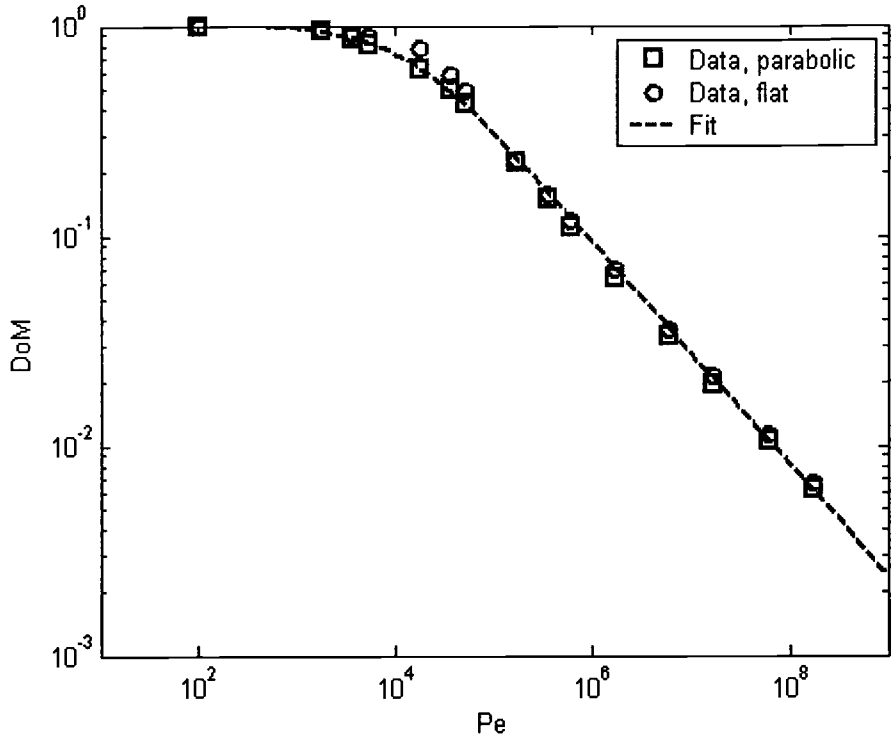

Figure 5.1 DoM vs. Pe for 2-D model

By presenting the data in this manner, two features become readily apparent. The first is the strong agreement between the results for the two velocity profiles. They are within 10% of each other, except at the shoulder of the curve near Peclet number of 10,000, where the difference is 25%.

The reason that DoM for the flat velocity profile is consistently higher than that for the parabolic profile is due to the difference in speed of the mixing zones in each profile. While the average speed is the same for the two profiles for a given mass flow rate, the local speed for the parabolic velocity profile is greater than that

of the flat profile for the central 58 percent of the channel. More importantly, this central 58 percent of the channel contains approximately 77 percent of the mass flow, with only 11.5 percent of the mass flow at each side of the channel being slower than the flat profile.

If the interfaces at which diffusive mixing takes place, hereafter referred to as mixing zones, are thought of as planes in the flow, they occur at even intervals of mass flow. In the third branch level, after one merging, a single mixing zone is located such that one half of the mass flow is on each side (i.e. in the center of the channel). In the second branching level, after two mergings, there are three mixing zones which separate the flow into four regions of equal mass flow. It is not until the zeroeth branching level, with zones dividing the mass flow into sixteenths, that mixing zones are formed in the region where the parabolic profile is slower than the flat profile, and then it is for only two out of the fifteen mixing zones.

The end result of this is, although the average speed is the same for the two profiles, that the speed of the fluid at the location of most of the mixing zones for a parabolic velocity profile is higher than that of a flat profile. Because of this increased speed, the time that the fluid at these mixing zones resides in the device is lower, hence allowing less mixing to occur.

The second feature on Figure 5.1 is the linear asymptotes (on a log-log plot) for the curve at high and low Peclet numbers. At low Peclet numbers, DoM approaches a constant value of 1. This is to be expected, as DoM = 1 represents complete mixing, and should be approached as the Peclet number approaches 0,

representing either still fluid or an infinitely diffusive solute. At high Peclet numbers, DoM approaches a power law. Curve fitting the data for Peclet numbers greater than 100,000 gives

$$DoM = 109 Pe^{-0.51} \tag{5-2}$$

This curve plotted along with the data is shown in Figure 5.2

The reason for the existence of a shoulder in the relationship between degree of mixing and Peclet number is related to how much mixing occurs in each

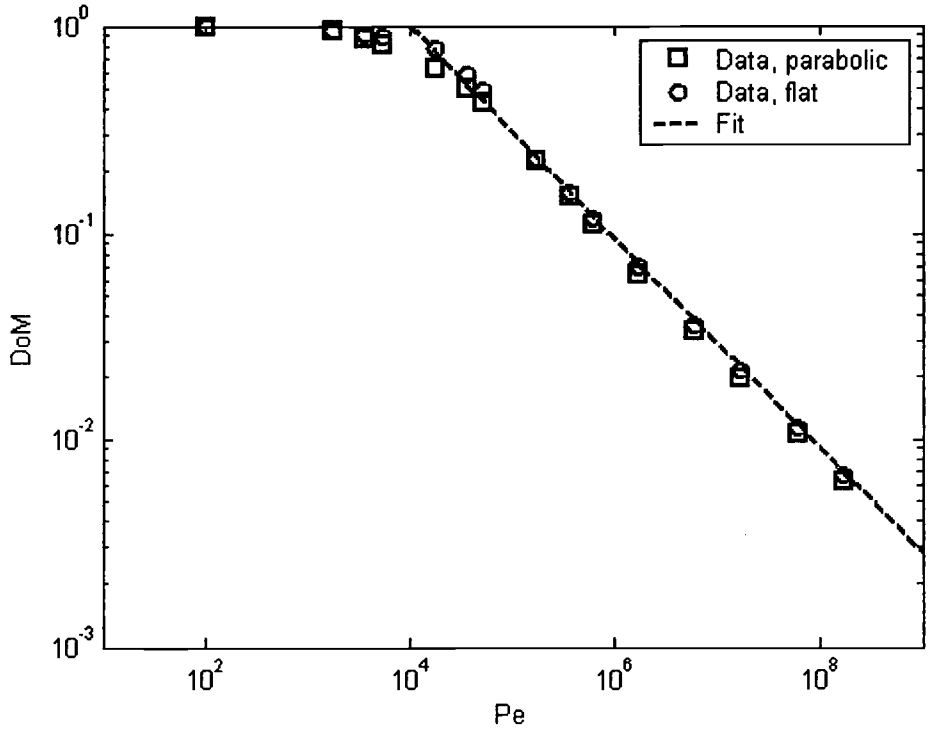

Figure 5.2 DoM vs. Pe for 2-D model with high Pe asymptote

branch level of the mixer. Figure 5.3 shows the degree of mixing at the exit from each branch level for the various values of Peclet number for each velocity profile. While the shape of the curves for Peclet numbers greater than 10^4 is relatively constant, being concave upwards, the curves for lower Peclet numbers are concave downwards.

Figure 5.4 shows this trend even more dramatically. In these figures, the degree of mixing at each branch level has been scaled by the degree of mixing at the exit from the 0^{th} branch level. When this is done, the high Peclet number curves collapse onto a single curve. For these curves, more mixing occurs in each subsequent branch level than in the previous branch level. However, for the low Peclet number curves, less mixing occurs in each branch than in the one before. The reason for this is quite simple: there is a finite limit to the amount of mixing that can occur. In the low Peclet number flows, so much mixing occurs in the early branches that there is little left to occur in the later branches.

The strength of this effect can be analyzed by comparing the distance over which the solute can diffuse while in a branching level of the network to the width of the concentration layers in that branch. The diffusion distance is proportional to the square root of the diffusivity multiplied by the residence time. The residence time, in turn, is the quotient of the length of the branching level and the average velocity in the level. The average width of a concentration layer is simply the width of the channel divided by the number of concentration layers in the channel.

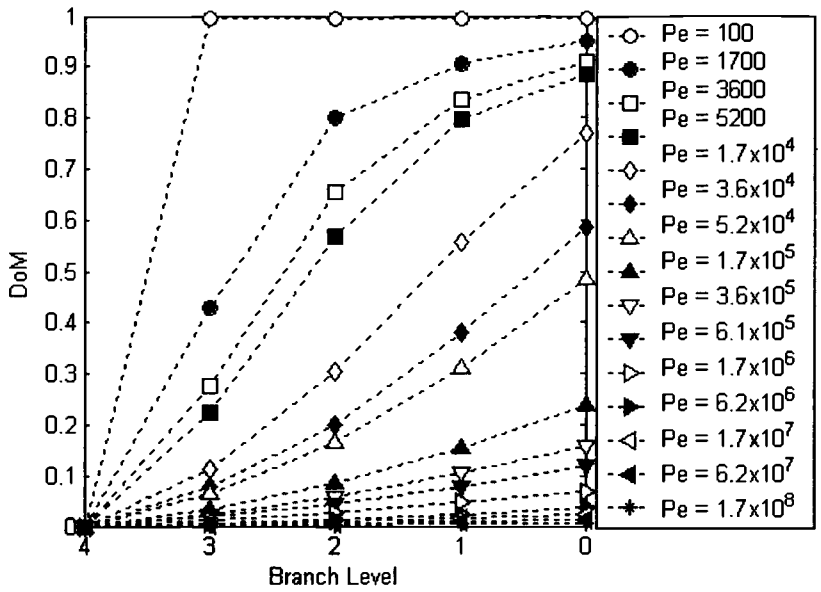

(a)

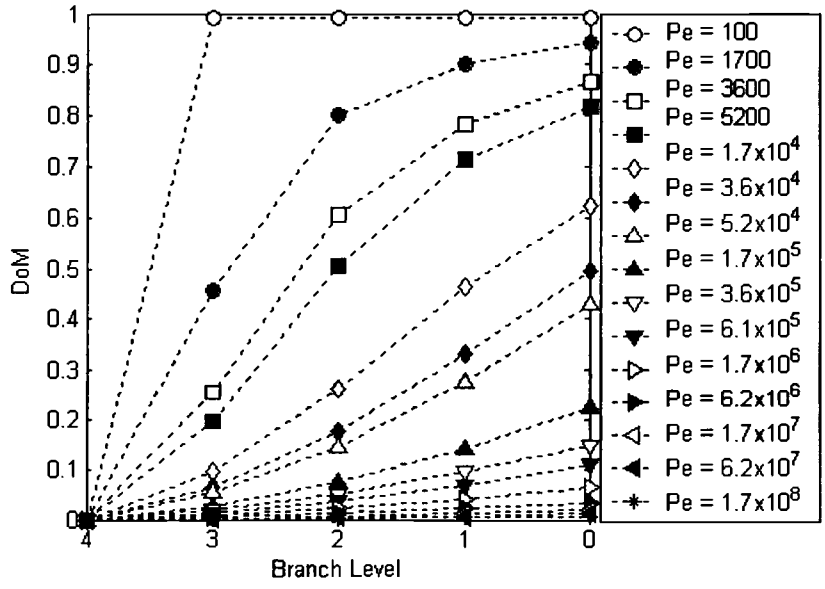

(b)

Figure 5.3 DoM vs. Branch Level
DoM at the exit of each branch level for (a) a flat velocity profile and (b) a parabolic velocity profile. The dotted lines are for ease of reference only.

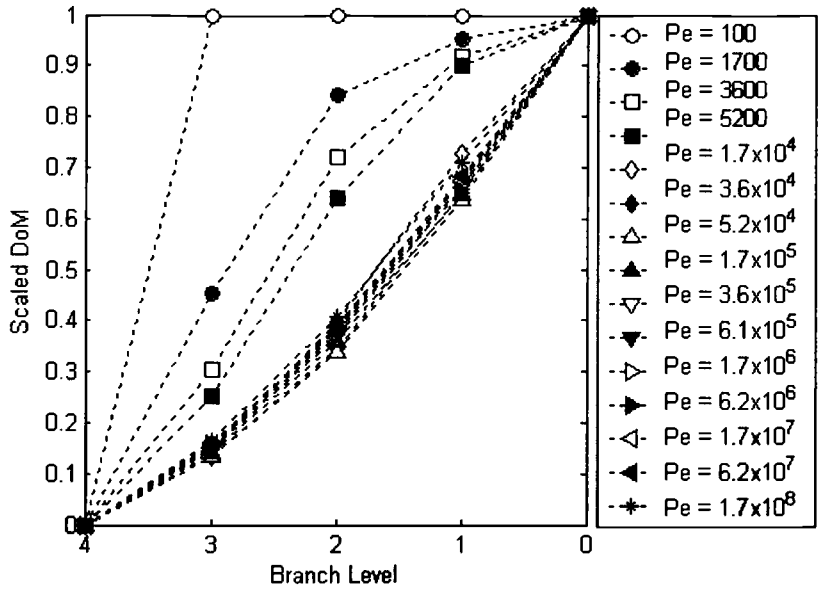

(a)

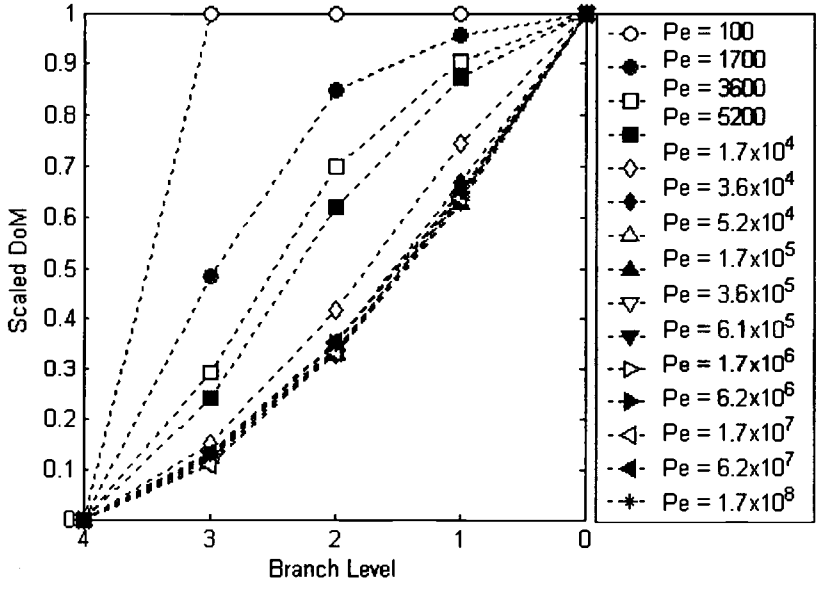

(b)

Figure 5.4 Scaled DoM vs. Branch Level
DoM at the exit of each branch level, divided by the DoM at the exit of the 0^{th} branch level for (a) a flat velocity profile and (b) a parabolic velocity profile. The dotted lines are for ease of reference only.

The ratio of these two quantities is

$$\frac{\sqrt{DL_k/V_k}}{w_k/2^{N-k}} \tag{5-3}$$

Because Peclet number is the descriptive parameter for the flow, mass diffusivity and velocity are not specified. However, their ratio is. Using the definition of the Peclet number and noting that for a constant density fluid, velocity ratios along a flow are the inverse of area ratios, the square of the numerator of Equation 5-3 can be rewritten as

$$\frac{DL_k}{V_k} = \frac{d_0 L_k A_k}{PeA_0} \tag{5-4}$$

Figure 5.5 shows the change in degree of mixing per branching level versus the quantity in Equation 5-3 for each Peclet number and branching level. Branching level increases from left to right. The four lowest Peclet numbers show a strong downturn in the change in degree of mixing per branching level when the quantity in Equation 5-3 increases past approximately 0.4

This indicates that there is an optimal Peclet number at which to run this specific device. For a given solute, and hence given Schmidt number, this results in an optimal Reynolds number. Running below the optimum Peclet number gives only small increases in the degree of mixing, while running above the optimum Peclet number results in significantly less mixing and increases in pumping power, due to the increased flow rate. Using the power law asymptote for the combined

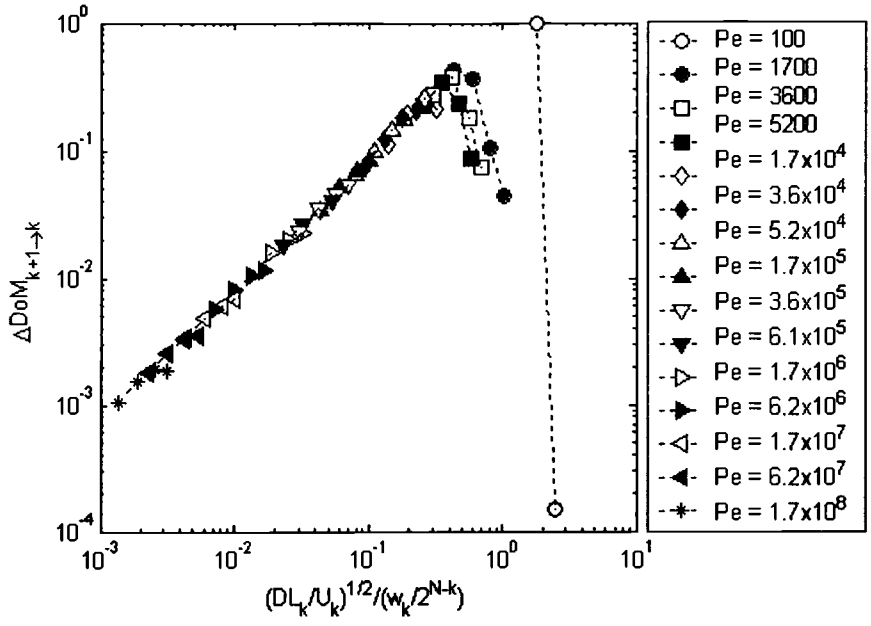

(a)

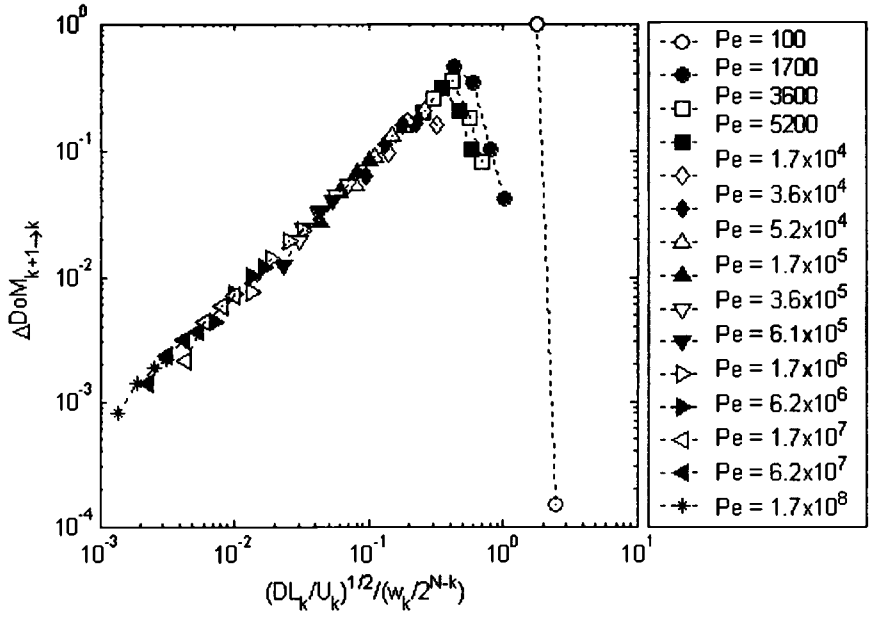

(b)

Figure 5.5 Change in DoM vs. Distance Ratio
Change in DoM per branch level versus the ratio of diffusion distance to concentration layer width for (a) a flat velocity profile and (b) a parabolic velocity profile. The dotted lines connect data for a constant Peclet number.

flat and parabolic velocity predictions for high Peclet number data, Equation 5-2, and solving for DoM = 1 gives Pe = 9169. Using this value in the curve fit to the combined parabolic and flat velocity profile data, Equation 5-1, give DoM = 0.744. So, the two-dimensional model predicts approximately 75 percent mixing at a Peclet number of about 9170. For solutes in water, where the Schmidt numbers are on the order of 10^3 to 10^4, this results in optimal Reynolds numbers of approximately 1 to 10 for this particular geometry.

Running at a Peclet number lower than this is entering into a region of strongly diminishing returns. While in the high Peclet number portion of the curve where the data can be approximated by a power law, i.e. above 10^5, halving the Peclet number gives an approximately 40 percent increase in the degree of mixing. However, from the optimum at Peclet number equal to 9170, halving the Peclet only results in a 14% increase in DoM. Moving to even lower Peclet numbers provides even less benefit.

5.2 PHYSICAL EXPERIMENT

The physical experiment was used to corroborate the results of the two-dimensional model. Figure 5.6 shows a comparison between the concentration profiles at the end of each branching level as predicted by the two-dimensional model and measured during the physical experiment. Although the span-wise locations of the peaks and valleys in the experimental profile show the same rough

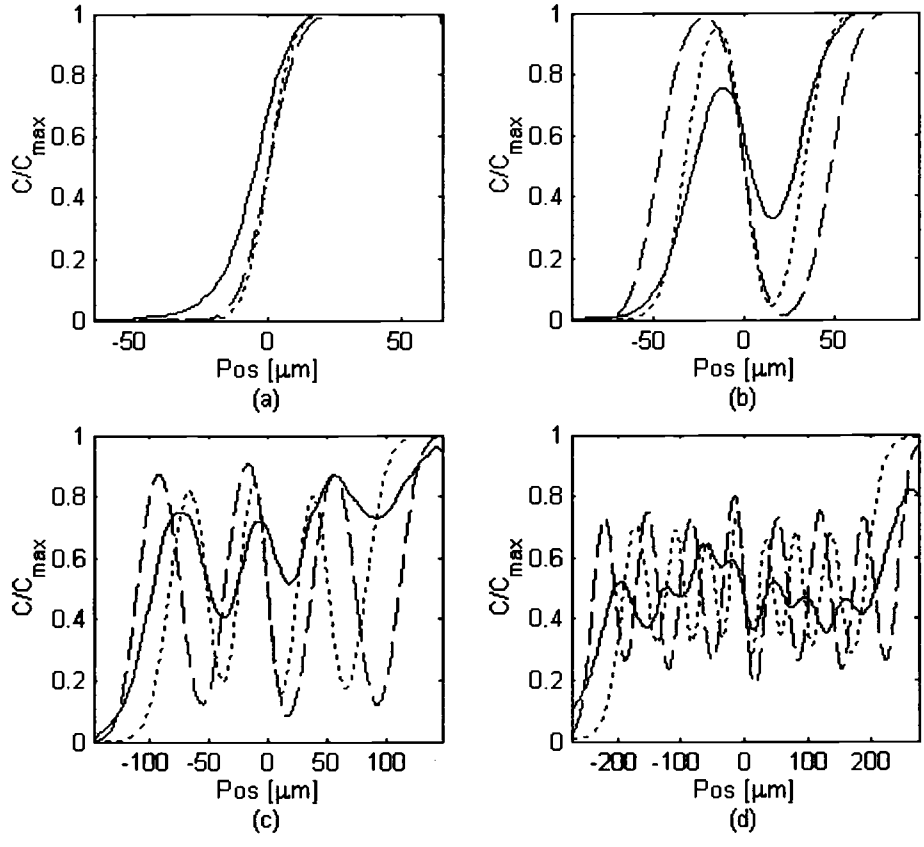

Figure 5.6 Comparison of Experiment and Two-Dimensional Model Profiles are at the end of (a) 3rd (b) 2nd (c) 1st and (d) 0th branching levels. In all four plots, the solid line is the experimental data, the dashed line is the flat velocity profile, and the dotted line is parabolic velocity profile.

trends as those of the profile generated using the parabolic velocity profile, the magnitude of these peaks and valleys do not agree as well.

The locations of the peaks and valleys in the concentration profiles are dependent upon the shape of the velocity profile. The velocity profile in turn is in turn dependent upon the level of flow development. A stronger agreement between

the experimental data and the predictions of the parabolic velocity profile indicates that the flow is close to being fully developed. A standard correlation (White, 1997) for prediction entry lengths of laminar flow in ducts was used and predicts lengths of 6 to 7 percent of the channel segment length for a Reynolds number of 10.

The disagreement in concentration magnitude between the two-dimensional model and the experiment is believed to be due to the three-dimensional nature of the flow. Because the entire channel is illuminated and fluoresces but is viewed from above, a sharp gradient that is not aligned vertically in the channel, such as that in the top of Figure 5.7 and resulting from the three-dimensionality of the flow, will appear the same as a larger zone of a smaller, horizontal gradient, such as that in the bottom of Figure 5.7. This increases the amount mixing that is measured experimentally.

Figure 5.8 shows degree of mixing versus Reynolds number for the two-dimensional model and the experiment, calculated using both Equations 4-5 and 4-6. The two-dimensional results are for both the flat and the parabolic velocity profiles. Degree of mixing using the average of the inlet concentrations, Equation 4-5, is almost constant with respect to Reynolds number, but when calculated using the measured average concentration, Equation 4-6, shows the same trend as that of the two-dimensional model, though the values themselves are different. The increase in mixing measured in the experiment is believed to be largely attributed to the bending of the mixing layers, as it is strongly Reynolds number dependent.

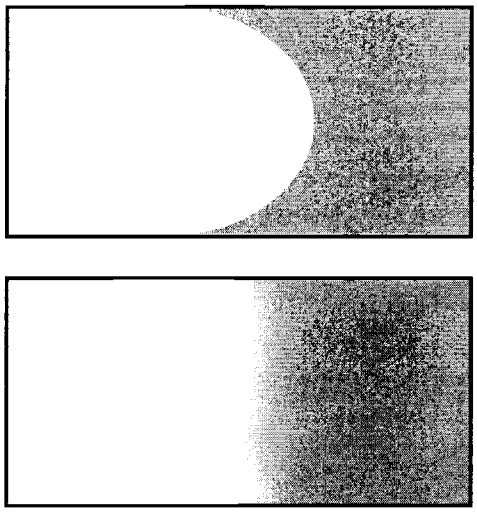

Figure 5.7 False Mixing from a Bent Mixing Zone
The two concentration distributions can appear the same when viewed from above, even though there is no actual mixing in the top one. Bending can occur due to the three-dimensionality of the flow.

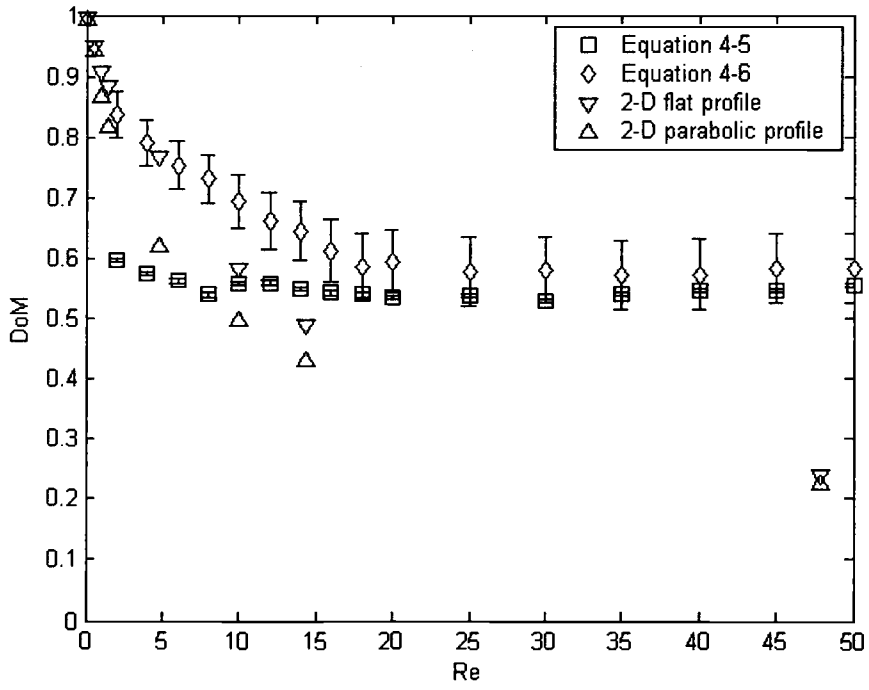

Figure 5.8 DoM vs. Re

Figure 5.9 shows the degree of mixing along the channel network from inlet to outlet for both velocity profiles employed in the two-dimensional model, along with that calculated from the experimental results, all for a Reynolds number of 10. The experimental data were gathered near the beginning, the middle, and the end of each of the branches of the zeroeth through second branching levels, and near the ends of the branches of the third branching level The model shows strong agreement between the two velocity profiles. However, as noted earlier, the degree of mixing is larger for the flat velocity profile than for the parabolic. At the exit of

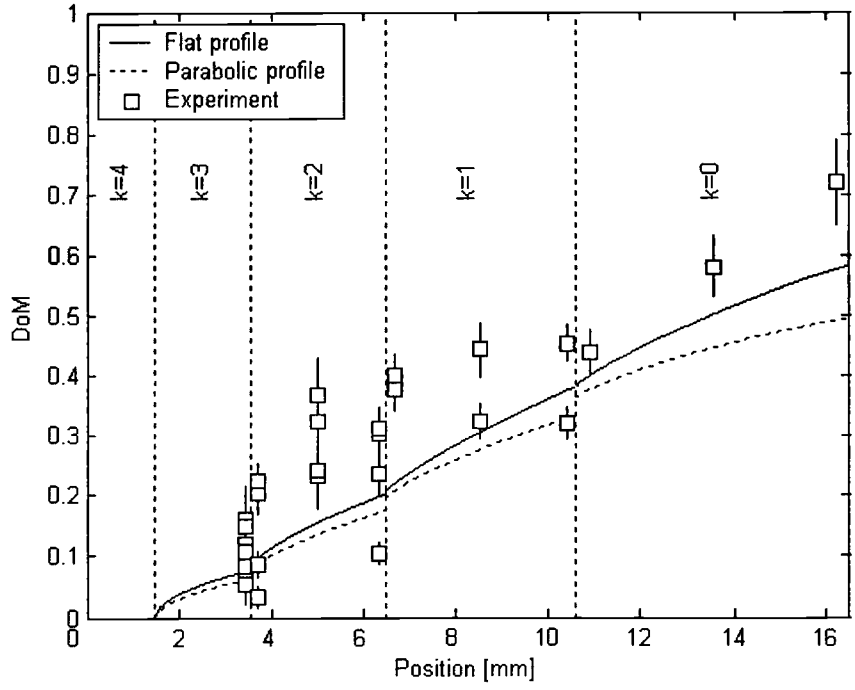

Figure 5.9 DoM vs. Position

the test section, the degree of mixing for the flat profile is 18 percent higher. The experimental data shows strong scattering. The model appears to under predict the experimental data, probably because it does not take into account the three-dimensionality of the flow field in the experimental test piece.

5.3 THREE-DIMENSIONAL CFD

The CFD model built in StarCD was used to examine the three-dimensionality of the velocity field inside the channel network and what effect this has on the mixing zones. Figure 5.10 shows the path of particles introduced at the junctions of the 4^{th} branching level segments, which correspond to the point where the first two dyed and non-dyed streams meet. At each junction, five particles are introduced evenly across the middle 80 percent of the channel depth. The particles are fictitious and simply mark streamlines in the flow. If the flow were in fact two-dimensional, the streamlines would be remain aligned in the z-direction through out the flow. As can be seen in Figure 5.10, this is not the case. While the distortion of the flow is small for Reynolds number equal to 1, 5, and 10, at Reynolds number equals 50, the distortion is significant.

Assuming these particles represent the interfaces between two diffusing concentration layers. The increased distortion for Reynolds number equal to 50 could account for an increase in the interfacial area across which diffusion takes place. As such, the two-dimensional model should slightly under predict the amount of mixing that occurs in high Reynolds number flows.

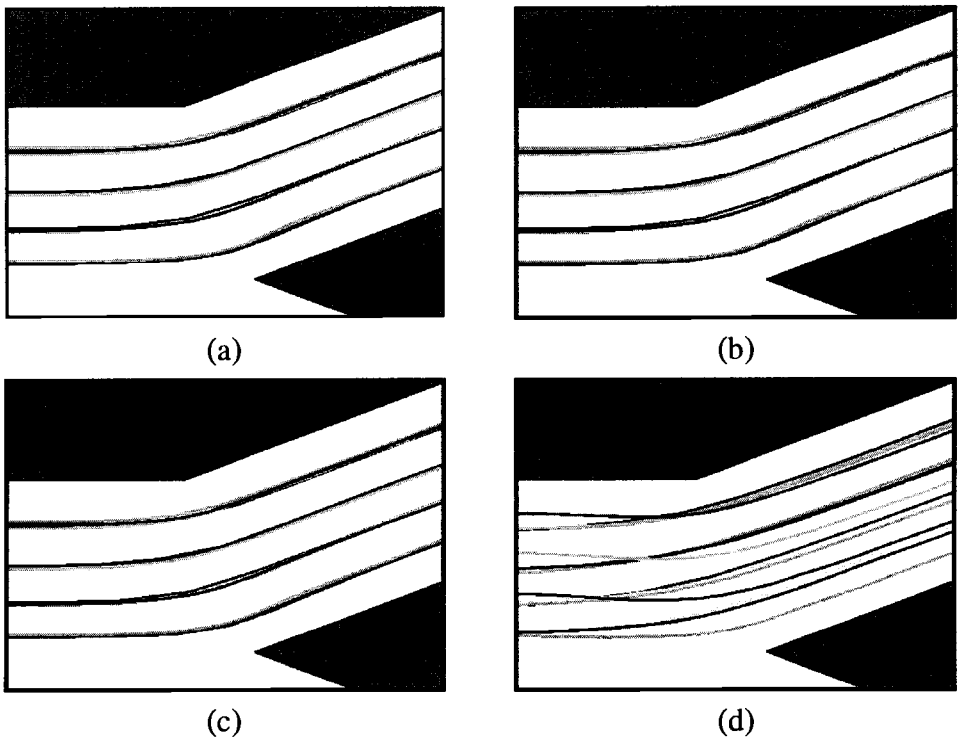

Figure 5.10 Mixing Layer Streamlines
Streamlines at entrance into 0^{th} level channel for (a) Re = 1 (b) Re = 5 (c) Re = 10 and (d) Re = 50.

5.4 TWO-DIMENSIONAL MODEL GEOMETRY VARIATION

Figure 5.11 shows DoM predicted using both flat and parabolic velocity profiles as a function of N for various values of L/h and w_N/h. As expected, DoM increases with increasing L/h and decreasing w_N/h, which correspond to longer residence times and decreased distances over which diffusion must take place,

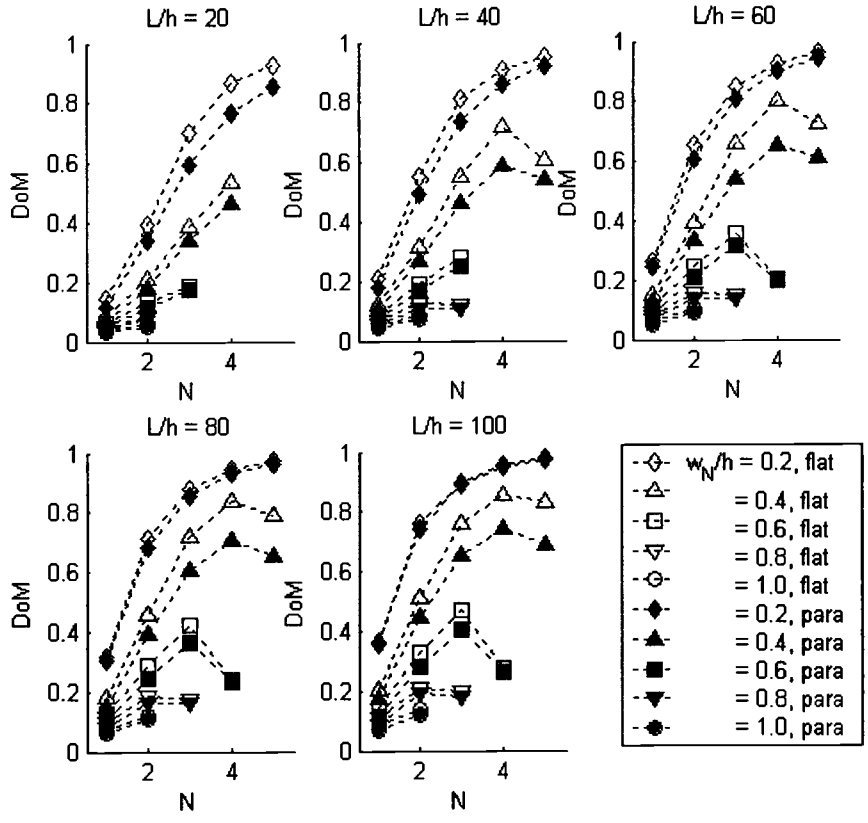

Figure 5.11 DoM vs. N for Varying L/h and w_N/h

respectively. DoM is expected to increase with increasing N, because of the increased number of mixing layers in the 0^{th} channel. However, as can be seen in Figure 5.11, it does so only up to a point.

Although the number of mixing layers increases with N, which should improve mixing, the width of the 0^{th} channel increases as well, which results in an increase then thickness of the concentration layers. Recalling the relationship between w_0, w_N, h, and β

$$w_0 = \frac{w_N h}{(w_N + h)\beta^N - w_N} \tag{5-5}$$

This increase in width can be offset by an increase in length, hence the point at which increasing N results in a decrease in DoM is dependent on length. Figure 5.12 shows Π versus N for varying w_N/h and L/h, where Π is defined as the ratio of the denominator of the Equation 5-5 over the total length

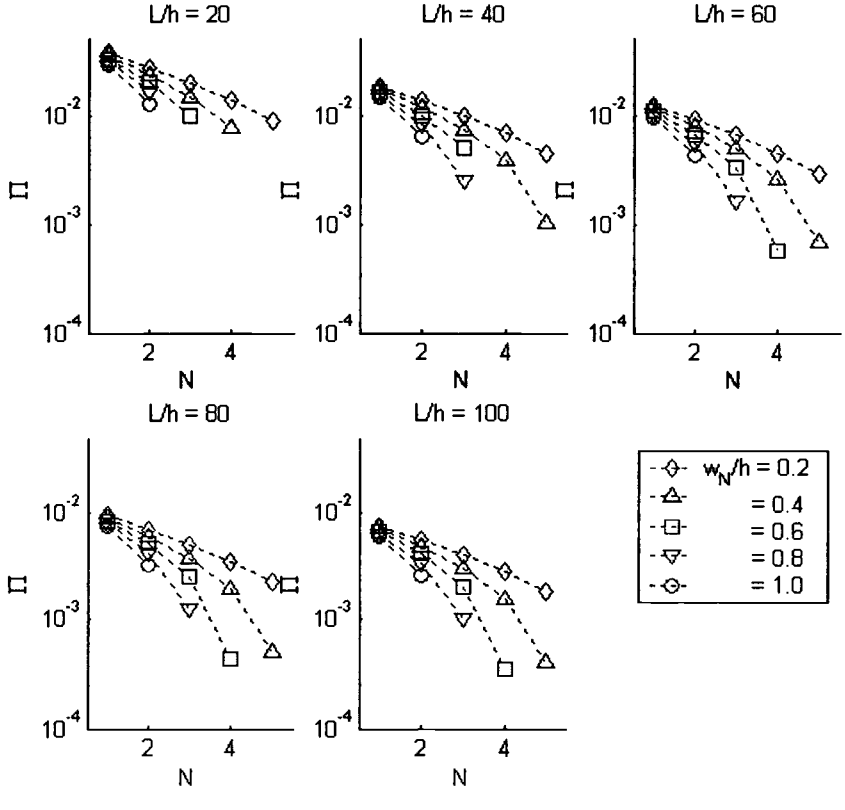

Figure 5.12 Π vs. N for Varying L/h and w_N/h

$$\Pi = \frac{(w_N + h)\beta^N - w_N}{L} \tag{5-6}$$

This is equivalent to the denominator of Equation 5-5 scaled by h over the parameter L/h.

By comparing Figures 5.11 and 5.12, it can be seen that Π less than or equal to 10^{-3} corresponds to those cases for which further increases in N result in decreases in DoM. This provides a critical Π value which can be used with Equation 5-6 to determine the optimum N as a function of L, h, and w_N. Rearranging Equation 5-6 and constraining Π to be less than the critical value yields the following inequality.

$$N \leq \frac{\log\left(\frac{w_N + \Pi_{crit} L}{w_N + h}\right)}{\log \beta} \tag{5-7}$$

Using the case where w_N/h is 0.6 and L/h is 80 as an example, wN is 150 μm, L is 20,000 μm, h is 250 μm, and β is $2^{-1/3}$. With a critical Π value of 10^{-3}, Equation 5-7 yields that N must be less than or equal to 3.7. As can be seen in Figure 5.11, for these values of w_N/h and L/h, N equal to 3 gives a higher degree of mixing than N equal to 4. For the case where w_N /h is 0.2 and L/h is 100, Equation 5-7 predicts that N should be less than or equal to 6.0 for a maximum degree of mixing.

Pumping power is also a consideration when evaluating the performance of a micro-mixer. The pressure drop through the device was predicted using the one-dimensional model formulated by Pence (2002), which assumes laminar flow with re-initiation of the hydrodynamic boundary layer following each merging and neglects minor losses. Figure 5.13 shows the pressure drop as a function of N, for varying L/h and w_N/h. As expected the pressure drop across the device decreases with shorter total length and wider channels. As can be seen in Figure 5.13, the

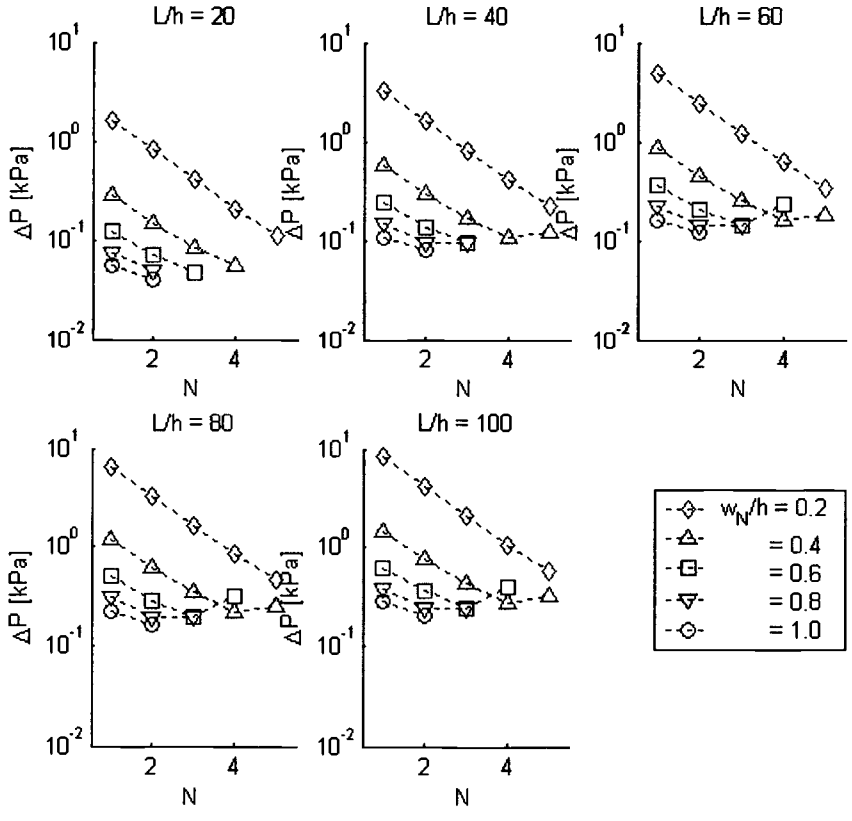

Figure 5.13 ΔP vs. N for Varying L/h and w_N/h

pressure drop shows similar behavior with respect to N as DoM does, namely that it decreases with N as long as Π does not become lower than 10^{-3}, at which point the pressure drop begins to increase.

Often more important than the pressure drop is the power required to pump fluid through the device. Figure 5.14 shows pumping power required as a function of N, for varying L/h and w_N/h. Pumping power is simply the sum of the pressure drop through each branching level multiplied by the volumetric flow rate and

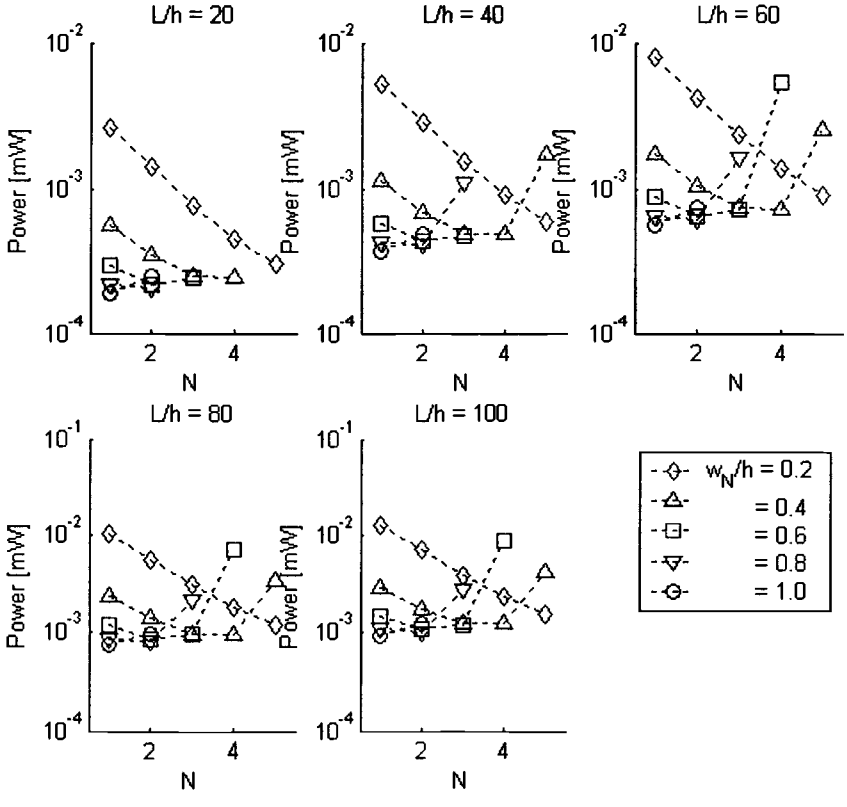

Figure 5.14 Pumping Power vs. N for Varying L/h and w_N/h

number of branches per level:

$$Power = \sum_{k=0}^{N} 2^k \Delta P_k Q_k \tag{5-8}$$

As expected, pumping power shows similar behavior as pressure drop. However, because of the changing number of branches, represented by the 2^k in Equation 5-8, power shows a more rapid increase than the pressure drop when Π_{crit} is reached.

Figure 5.15 shows the ratio of DoM to pumping power as a function of N, for varying L/h and w_N/h. Because of the strong dependence of both DoM and power on Π, this ratio decreases very rapidly once Π_{crit} is reached. Beyond Π_{crit}, the performance of the mixer drops rapidly.

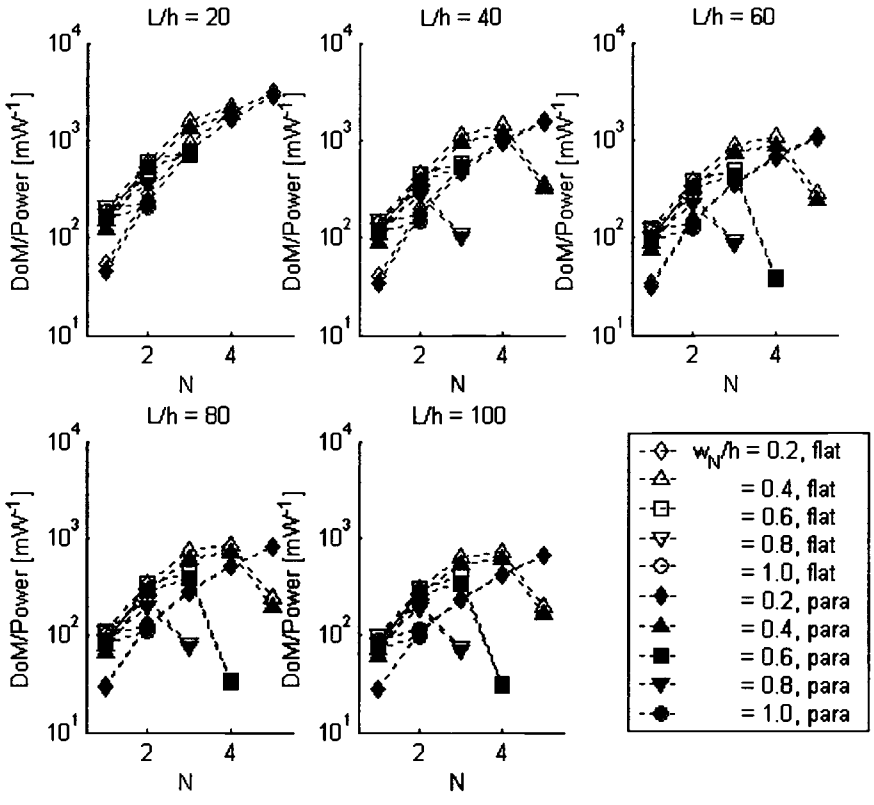

Figure 5.15 Ratio of DoM to Pumping Power vs. N for Varying L/h and w_N/h

6. CONCLUSIONS AND RECOMMENDATIONS

A two-dimensional model with two different specified velocity profiles was used to predict the concentration profiles and degree of mixing at the exit of a fractal-like merging channel network. This model predicts a dependence of degree of mixing on Peclet number that has an asymptotic approach to 1 for Peclet numbers less than 10^3 and an inverse power law asymptote for Peclet numbers higher than 10^5. The two-dimensional model predicts an optimal Peclet number of approximately 9200 to achieve a maximum amount of mixing for the flow network considered.

A physical experiment was used to confirm the results of the two-dimensional model. The amount of mixing measured in the experiment exceeded that predicted by the two-dimensional model

CFD was used to examine the three-dimensionality of the flow field, and the effects this has on the mixing zones. At low Reynolds numbers, the particle tracks indicates that the flow field does not exhibit strong secondary effects. However, for Reynolds numbers of 50 and higher, the velocity field becomes more strongly three-dimensional, resulting in bending of the mixing zones.

The two-dimensional model was also used to predict the effects of geometry variation. Increased length and decreased width both increased the amount of mixing. This was expected as these correspond to increased residence time and

decreased diffusion distance, respectively. Increasing the number of branching levels also increased the degree of mixing, but only up to a point. If the number of branching levels is increased too much, the maintenance of the constant ratio of hydraulic diameters between branching levels, when combined with the fixed depth of the device, results in an excessively wide final channel in the 0^{th} branching level. This increase in width more than offsets the gain from the corresponding increase in the number of mixing layers. A non-dimensional parameter was defined that predicts an optimum number of branching levels for given inlet channel width, channel depth, and total length.

Because this study is finite in scope, there are several unresolved issues. Hence, there are the following recommendations:

- The geometry of the device used in this study was not optimized for mixing. Hence, in future studies an optimized geometry should be used.
- In this study, geometry variations were only studied in how they effected the degree of mixing for a fixed Peclet number. The effect upon optimum Peclet number and upon the degree of mixing at this optimum should be investigated.
- Because the data obtained in the physical experiment was strongly effected by the three-dimensionality of the flow, in future studies a reacting flow should be used, so that only the effects of actual mixing are measured.
- To more accurately examine the curving of the mixing zones and to corroborate the two-dimensional model, the concentration field should be analyzed in the three-dimensional CFD model.

REFERENCES

Alharbi, A., 2001, "A Study of Micro-Scale, Fractal-Like Branching Flow Networks for Reduced Pumping Power and Improved Temperature Uniformity," M.S. Thesis, Oregon State University, Corvallis, OR.

Bejan, A., "Constructal Tree Network for Fluid Flow Between a Finite-Size Volume and One Source or Sink," Revue Générale de Thermique, **36**, pp. 592-604.

Branebjerg, J., Gravesen, P., Krog, J. P., and Nielsen, C. R., 1996, "Fast Mixing by Lamination," Proceedings of the IEEE Micro Electro Mechanical Systems (MEMS), pp 441-446.

Chapra, S. C., and Canale, R. P., 1998, "Numerical Methods for Engineers with Programming Software Applications: Third Edition," McGraw-Hill.

Ehlers, S., Elgeti, K., Menzel, T., Wiessmeier, G., 2000, "Mixing in the offstream of a microchannel system," Chemical Engineering and Processing, **39**, pp 291-298.

Ismagilov, R. F., Stroock, A. D., Kenis, P. J. A., Whitesides, G., and Stone, H. A., 2000, "Experimental and Theoretical Scaling Laws for Transverse Diffusive Broadening in Two-Phase Laminar Flows in Microchannels," Applied Physics Letters, **76**, 17, pp 2376-2378.

Ju, Y. S., 2000, "Thermal Conduction and Viscous Heating in Microscale Couette Flows," Journal of Heat Transfer, **122**, pp 817-818.

Kamholz, A. E., Schilling, E. A., Yager, P., 2001 "Optical Measurement of Transverse Molecular Diffusion in a Microchannel," Biophysical Journal, **80**, pp 1967-1972.

Kenis, P. J. A., Ismagilov, Whitesides, G. M., 1999 "Microfabrication Inside Capillaries Using Multiphase Laminar Flow Patterning," Science, **285**, 2, pp 83-85.

Liu, R. H., Stremler, M. A., Sharp, K. V., Olsen, M. G., Santiago, J. G., Adrian, R. J., Aref, H., and Beebe, D. J., 2000, "Passive Mixing in a Three-Dimensional Serpentine Microchannel," Journal of Microelectromechanical Systems, **9**, 2, pp 190-197.

Lorente, S., Wechsatol, W., Bejan, A., 2002, "Tree-Shaped Flow Structures Designed by Minimizing Path Lengths," International Journal of Heat and Mass Transfer, **45**, pp 3299-3312.

Nelson, T. R., West, B. J, Goldberger, A. L., "The Fractal Lung: Universal and Species-Related Scaling Patterns," Experientia, **46**, pp 251-254.

Pence, D. V., 2000, "Improved Thermal Efficiency and Temperature Uniformity Using Fractal-Like Branching Channel Networks," Proceedings of the International Conference on Heat Transfer and Transport Phenomena in Micro Scale, Banff, Canada, pp 142-148.

Pence, D. V., 2002, "Reduced Pumping Power and Wall Temperature in Microchannel Heat Sinks with Fractal-Like Branching Channel Networks," Microscale Thermophysical Engineering, **6**, 4, pp. 319-330.

Stroock, A D, Dertinger, S K W, Ajdari, A, Mezic, I, Stone, H A, Whitesides, G. M, 2002, "Chaotic Mixer for Microchannels," Science, **295**, 25 January, pp 647-651.

Tannehill, J. C., Anderson, D. A., Pletcher, R. H., 1997, "Computation Fluid Mechanics and Hear Transfer: Second Edition," Taylor & Francis.

Volpert, M., Meainhart, C. D., Mezic, I., Dahleh, M., 1999, "An Actively Controlled Micromixer," Microelectromechanical Systems (MEMS), **1**, pp 483-487.

West, G. B., Brown, J. H., Enquist, B. J., 1997, "A General Model for the Origin of Allometric Scaling Laws in Biology," Science, **276**, 4, pp 122-126.

White, F. M., 1991 "Viscous Fluid Flow: Second Edition," McGraw-Hill.

Yang, J., Huang, Y., Wang, X., Becker, F. F., Gascoyne, P. R. C., 2000, "Differential Analysis of Human Leukocytes by Dielectrophoretic Field-Flow-Fractionation," Biophysical Journal, **78**, pp 2680-2689.

APPENDICES

APPENDIX A: ERROR ANALYSIS

For measured quantities, uncertainty in the measurement was estimated. For calculated quantities, uncertainty was estimated using the Kline-McClintock relationship.

$$f = f(x_1, x_2, \ldots, x_m) \tag{A-1}$$

$$\delta f = \sqrt{\left(\delta x_1 \frac{\partial f}{\partial x_1}\right)^2 + \left(\delta x_2 \frac{\partial f}{\partial x_2}\right)^2 + \ldots \left(\delta x_m \frac{\partial f}{\partial x_m}\right)^2} \tag{A-2}$$

A.1 TWO-DIMENSIONAL MODEL

In the two-dimensional model, the criterion for grid-independence is when halving of the grid spacing results in a relative change in DoM of less than 0.01. This was then taken as the uncertainty in DoM.

The uncertainty in the local scaled concentration was then the standard deviation between the concentration profile generated using the most refined and second-most refined grids. These values are less than 0.04. It should be noted that this error is largely the result of small shifts in the location of high gradient areas.

A.2 THREE-DIMENSIONAL CFD

The error in the velocity field generated using StarCD was estimated using StarCD's built in error estimation feature. It estimates the effects of grid spacing, irregularity, and non-orthogonality and advection differencing scheme. This error estimation is based on the local imbalance between face interpolation and volume integration. The velocity error estimate contains the error estimate of the pressure field as well. The grid was refined in areas of high error until the relative error was less than 2.5 percent.

A.3 PHYSICAL EXPERIMENT

The uncertainty in the local concentration was estimated by the standard deviation of the data used to generate the concentration calibration curve from the fitted curve. This value is 0.03.

For discrete quantities, DoM is defined by

$$DoM = 1 - \frac{1}{\overline{C}} \left\{ \frac{1}{m} \sum_{j=1}^{m} \left[C_j - \overline{C} \right]^2 \right\}^{\frac{1}{2}} \qquad \text{(A-3)}$$

By Kline-McClintock, the error in DoM is given by

$$\delta DoM = \left[\sum_{i=1}^{m} \left(\delta C_i \frac{\partial DoM}{dC_i} \right)^2 + \left(\delta \overline{C} \frac{\partial DoM}{d\overline{C}} \right)^2 \right]^{\frac{1}{2}} \quad \text{(A-4)}$$

Because the uncertainty in the concentration is independent of concentration, this becomes

$$\delta DoM = \left[\delta C^2 \sum_{i=1}^{m} \left(\frac{\partial DoM}{dC_j} \right)^2 + \left(\delta \overline{C} \frac{\partial DoM}{d\overline{C}} \right)^2 \right]^{\frac{1}{2}} \quad \text{(A-5)}$$

The partial derivatives are

$$\frac{\partial DoM}{dC_i} = -\frac{1}{m\overline{C}} \left(C_i - \overline{C} \right) \left[\frac{1}{m} \sum_{j=1}^{m} \left[C_j - \overline{C} \right]^2 \right]^{-\frac{1}{2}} \quad \text{(A-6)}$$

$$\frac{\partial DoM}{d\overline{C}} = \frac{1}{\overline{C}^2} \left\{ \frac{1}{m} \sum_{j=1}^{m} \left[C_j - \overline{C} \right]^2 \right\}^{\frac{1}{2}} \quad \text{(A-7)}$$

Using the definition of the arithmetic mean

$$\overline{C} = \frac{1}{m} \sum_{j=1}^{m} C_j \quad \text{(A-8)}$$

and Kline-McClintock

$$\delta \overline{C} = \left[\sum_{i=1}^{m} \left(\delta C_i \frac{\partial \overline{C}}{dC_i} \right)^2 \right]^{\frac{1}{2}} = \left[\delta C^2 \sum_{i=1}^{m} \left(\frac{\partial \overline{C}}{dC_i} \right)^2 \right]^{\frac{1}{2}} = \delta C \left[\sum_{i=1}^{m} \left(\frac{\partial \overline{C}}{dC_i} \right)^2 \right]^{\frac{1}{2}} = \delta C \sqrt{m} \quad \text{(A-9)}$$

So

$$\left(\delta\overline{C}\frac{\partial DoM}{d\overline{C}}\right)^2=\left(\frac{\delta C\sqrt{m}}{\overline{C}^2}\left\{\frac{1}{m}\sum_{j=1}^{m}\left[C_j-\overline{C}\right]^2\right\}^{\frac{1}{2}}\right)^2=\frac{\delta C^2}{\overline{C}^4}\sum_{j=1}^{m}\left[C_j-\overline{C}\right]^2 \qquad \text{(A-10)}$$

and

$$\begin{aligned}\delta C^2\sum_{i=1}^{m}\left(\frac{\partial DoM}{dC_i}\right)^2&=\delta C^2\sum_{i=1}^{m}\left(\frac{\left(C_i-\overline{C}\right)}{m\overline{C}}\left[\frac{1}{m}\sum_{j=1}^{m}\left[C_j-\overline{C}\right]^2\right]^{-\frac{1}{2}}\right)^2\\&=\frac{\delta C^2}{m^2\overline{C}^2}\left[\frac{1}{m}\sum_{j=1}^{m}\left[C_j-\overline{C}\right]^2\right]^{-1}\sum_{i=1}^{m}\left(C_i-\overline{C}\right)^2\\&=\frac{\delta C^2}{m\overline{C}^2}\end{aligned} \qquad \text{(A-11)}$$

Putting it altogether gives

$$\begin{aligned}\delta DoM&=\left[\frac{\delta C^2}{m\overline{C}^2}+\frac{\delta C^2}{\overline{C}^4}\sum_{j=1}^{m}\left[C_j-\overline{C}\right]^2\right]^{\frac{1}{2}}\\&=\left[\frac{1}{m}+\frac{1}{\overline{C}^2}\sum_{j=1}^{m}\left[C_j-\overline{C}\right]^2\right]^{\frac{1}{2}}\frac{\delta C}{\overline{C}}\end{aligned} \qquad \text{(A-12)}$$

The remaining sum is simply the standard variance in C multiplied by m, so it can be approximated by the uncertainty in C squared and multiplied by m

$$\delta DoM=\left[\frac{1}{m}+\frac{m\delta C^2}{\overline{C}^2}\right]^{\frac{1}{2}}\frac{\delta C}{\overline{C}} \qquad \text{(A-13)}$$

For those calculations in which the average scaled concentration is specified, there is no uncertainty in the average, so the second term disappears

$$\delta DoM = \frac{\delta C}{\overline{C}\sqrt{m}} \qquad \text{(A-14)}$$

APPENDIX B: MATLAB CODE

Many of the calculations in this study were performed using the software package Matlab. The two-dimensional model was done entirely in Matlab.

B.1 TWO-DIMENSIONAL MODEL

The main codes used in the two-dimensional model were those used to calculate the concentration distribution in the channel network. The following code was used in the flow variation portion of the study and uses the parabolic velocity profile.

```
% Two dimensional mixing model for fractal branching network.
% Kent Enfield

clear C Cin w x y b V Cend
tic
% Problem Parameters
h0 = 250;      %Height of 0th branch in microns
w0 = 542.5;    %Width of 0th branch in microns
L0 = 5870;     %Length of 0th branch in microns
n = 4;         %Number of bifurcations
Re = 100;      %Reynolds number in largest (final) channel.
Ca = 1;        %Concentration in "A" channels in kg/m^3
Cb = 0;        %Concentration in "B" channels in kg/m^3
D = 2.8e-10;   %Binary diffusion coeffient in m^2/s.
nu =1.005e-6; %Kinematic viscocity of liquid in m^2/s.

Qtot = 0.5*Re*nu*(h0+w0);
Cin = zeros(1,2^n);
Cin(1:2:end) = Ca;
Cin(2:2:end) = Cb;
```

```
% Numerical parameters.
nx = 201;       %Number of divisions of each branch in lengthwise
direction.
ny = 801;       %Number of divisions of each branch in cross-channel
direction.
               %ny must be odd.
tol = 1e-5;    %solution error tolerance level

% Fractal characteristics:
beta = 2^(-1/3);     %hydraulic diameter ratio
gamma = 2^(-1/2);    %Length ratio

% Geometry generation
L = L0*gamma.^[0:n];
w = w0*ones(1,1+n);
for k = 1:n
    w(k+1) = beta*h0*w(k)/((1-beta)*w(k)+h0);
end

for i = 1:n+1
    x(i,1:nx+1) = [0:nx]*L(i)/nx;
    y(i,1:ny+1) = ([0:ny]-ny/2)*w(i)/ny;
end

b = D*(L/nx)./(w/ny).^2;

% Velocity profile generation
% (assumes parabolic profile everywhere)
Vave = Qtot./((w.*2.^[0:n])*h0);
for i = 1:n+1
    V(i,1:ny+1) = -1.5*Vave(i)*(1-4*(y(i,:)/w(i)).^2);
    % V is negative because flows from right to left (against +x
direction).
end

% Checking stability
% NOTE because D is so small, this is almost always stable (<= 0.5)

test = -max(b)/min(min(V(:,2:end-1)));
disp(' ')
disp(['Diffusion number = ',num2str(test),'.'])
if test >= 0.5
    disp('Solution unstable.  Change parameters.')
    disp(' ')
    return
elseif test >= 0.45
    disp('Solution barely stable.  Results may be unreliable.')
else
    disp('Solution stable.')
end
disp(' ')

%Generation of concentration solution arrays.
```

```
%    Solution array is of the form:
%       C(k,,x,y) = concetration
%    where
%       k is branch level (0,..,n) +1
%       x is x location
%       y is y location
C = ones(n,nx+1,ny+1);

% applying concentration inlet boundary condition.
C(end,end,1:(ny+1)/2) = Ca;
C(end,end,1:1+(ny+1)/2) = Cb;


% Solver
time =
clock;disp(strcat(num2str(round(time(4))),':',num2str(round(time(5)
)),':',num2str(round(time(6)))))
for k = n:-1:1

    disp(strcat('Now solving branch level=',num2str(k),'.'));

    if k ~= n
       % The following section maps one branch level onto the next
       % using conservation of mass, which becomes V*dw, due to
       % constant density and channel depth.
       for i = 1:ny+1
          XX(i) = w(k+1)*sum(V(k+1,1:i));
          X2(i) = w(k)*sum(V(k,1:i));
       end
       XX(end) = XX(end-1)*1.0000001;
       YY(1:ny+1) = C(k+1,1,1:ny+1);
       for i = 1:(ny+1)/2
          C(k,end,i) = interp1(XX,YY,X2(i));
       end
       for i = ((ny+1)/2)+1:ny+1
          C(k,end,i) = interp1(XX+XX(end),YY,X2(i));
       end

       clear XX X2 YY

    end

    for xi = nx:-1:1
        err = 1;
        C(k,xi,:) = C(k,xi+1,:);
        while err > tol
            Cold(1:ny+1) = C(k,xi,1:ny+1);

        C(k,xi,1) = (4*C(k,xi,2)-C(k,xi,3))/3;
        for yi = 2:ny
            C(k,xi,yi) = (b(k)*(C(k,xi,yi+1)+C(k,xi,yi-1))-
V(k,yi)*C(k,xi+1,yi))/(2*b(k)-V(k,yi));
        end
```

```
        C(k,xi,ny+1) = (4*C(k,xi,ny)-C(k,xi,ny-1))/3;

            Cnew(1:ny+1) = C(k,xi,1:ny+1);
            err = max(abs( (Cnew-Cold)./(Cold+eps)));
        end

    end

Cend(1:ny+1) = C(k,1,1:ny+1);

dCrms = 1-sqrt(sum((Cend - 0.5*(Ca+Cb)).^2)/ny)/(0.5*(Ca-Cb));
disp(strcat('DoM = ',num2str(dCrms)))

figure
plot(y(1,:),Cend,'r-x')
xlim([y(1,1) y(1,end)])
ylim([0 1])
xlabel('Cross-channel distance [\mum]')
ylabel('Concentration [kg/m^3]')
title(strvcat(['Concentration vs. Crosswise Position (at exit of
branch ',num2str(k-1),')'],...
    ['Pe= ',num2str(Re*nu/D),', parabolic velocity profile'],...
    strcat('              DoM = ',num2str(dCrms))))
set(gcf,'Color','w')

time =
clock;disp(strcat(num2str(round(time(4))),':',num2str(round(time(5)
)),':',num2str(round(time(6)))))
end

toc
```

The code using the flat velocity profile is identical except that

```
Vave = Qtot./((w.*2.^[0:n])*h0);
for i = 1:n+1
    V(i,1:ny+1) = -1.5*Vave(i)*(1-4*(y(i,:)/w(i)).^2);
    % V is negative because flows from right to left (against +x
direction).
end
```

is replaced with

```
Vave = Qtot./((w.*2.^[0:n])*h0);
```

```
for i = 1:n+1
    V(i) = -Vave(i);
    % V is negative because flows from right to left (against +x
direction).
end
```

The codes used in the geometry variation portion of the study are identical to the codes used for flow variation, except that

```
L0 = 5870;     %Length of 0th branch in microns
```

and

```
L = L0*gamma.^[0:n];
```

are replaced with

```
Lt = 5000;     %Total length of all branches in microns
```

and

```
L = Lt*(gamma.^[0:n])/sum(gamma.^[0:n]);
```

respectively.

B.2 PHYSICAL EXPERIMENT

Matlab was also used to convert the channel images into concentration data. The following code loads a series of images, filters them, averages them, and converts them into concentration data.

```
clear IMGARR

a = 3.5192e-5;
b = 1.9804;

n=6;
first=input('Basename of image sets   ');

for i=1:n;
    last=num2str(i-1);
    if i<10
        name=[first  '000' last];
    else
        name=[first  '00'  last];
    end

    I=avefilt(imread(name,'tif'),[2 5]);
    IMGARR(:,:,1,i)=I;
end

aveimg = double(mean(IMGARR,4));

conc = flipud(a*aveimg.^b);
figure
surf(conc)
set(gca,'clim',[0 1])
axis equal tight
shading interp
view(2)
```

The code above makes use of the following function to average the image data.

```
function C = avefilt(A,x)
%This function filters matrix A by averaging it over the distance
x.
[m n] = size(A);
B = zeros([m n]+2*x);
B(x(1)+1:x(1)+m,x(2)+1:x(2)+n) = A;
B(1:x(1)+1,1:x(2)+1)              = A(1,1);
B(1:x(1)+1,end-x(2):end)        = A(1,end);
B(end-x(1):end,1:x(2)+1)        = A(end,1);
B(end-x(1):end,end-x(2):end) = A(end,end);
for i = 1:x(1)
   B(x(1)+2:end-x(1)-1,i) = A(2:end-1,1);
   B(x(1)+2:end-x(1)-1,end+1-i) = A(2:end-1,end);
end
for j = 1:x(2)
   B(j,x(2)+2:end-x(2)-1) = A(1,2:end-1);
   B(end+1-j,x(2)+2:end-x(2)-1) = A(end,2:end-1);
end
C = zeros(m,n);
N = (2*x(1)+1)*(2*x(2)+1);
for i = -x(1):x(1)
   for j = -x(2):x(2)
      C = C+B(x(1)+1+i:m+x(1)+i,x(2)+1+j:x(2)+n+j);
   end
end
C = uint8(C/N);
```